

PHOTON AXION CONVERSION UNDER A STATIC MAGNETIC FIELD

By

SHAHAD HUSSAIN K S

DU2019MSC0067

DEPARTMENT OF PHYSICS

A THESIS

SUBMITTED

IN PARTIAL FULFILLMENT OF THE REQUIREMENT
FOR THE DEGREE OF

MASTER OF SCIENCE

IN PHYSICS

To



ASSAM DON BOSCO UNIVERSITY

TAPESIA GARDENS, TAPESIA,

SONAPUR – 782 402

ASSAM – INDIA

JULY, 2021

PHOTON AXION CONVERSION UNDER A STATIC MAGNETIC FIELD

By

SHAHAD HUSSAIN K S

DU2019MSC0067

DEPARTMENT OF PHYSICS

A THESIS

SUBMITTED

IN PARTIAL FULFILLMENT OF THE REQUIREMENT

FOR THE DEGREE OF

MASTER OF SCIENCE

IN PHYSICS

To



ASSAM DON BOSCO UNIVERSITY

TAPESIA GARDENS, TAPESIA,

SONAPUR – 782 402

ASSAM – INDIA



Department of Physics
School of Fundamental & Applied
Sciences
Assam Don Bosco University
Tapesia, Sonapur – 782 402

CERTIFICATE

This is to certify that this report titled

PHOTON AXION CONVERSION UNDER A STATIC MAGNETIC FIELD

is a bonafide record of the project work done by **Mr. Shahad Hussain K S** (Student ID DU2019MSC0067) at the Department of Physics, School of Fundamental & Applied Sciences, Assam Don Bosco University, under the guidance of **Dr. Debajyoti Dutta**, in partial fulfillment of the requirements of the *PSPR6012: Project Work* of the M.Sc. (Physics) curriculum.

Project Guide

Dr. Debajyoti Dutta

Place: ADBU, Tapesia

Date: July, 2021



Department of Physics
School of Fundamental & Applied
Sciences
Assam Don Bosco University
Tapesia, Sonapur – 782 402

CERTIFICATE

This is to certify that this report titled

PHOTON AXION CONVERSION UNDER A STATIC MAGNETIC FIELD

is a bonafide record of the project work done by **Mr. Shahad Hussain K S** (Student ID DU2019MSC0067) at the Department of Physics, School of Fundamental & Applied Sciences, Assam Don Bosco University, under the guidance of **Dr. Debajyoti Dutta**, in partial fulfillment of the requirements of the *PSPR6012: Project Work* of the M.Sc. (Physics) curriculum.

Head of the Department

Dr. Ngangom Aomoa

Place: ADBU, Tapesia

Date: July, 2021



Department of Physics
School of Fundamental & Applied
Sciences
Assam Don Bosco University
Tapesia, Sonapur – 782 402

CERTIFICATE

This is to certify that this report titled

PHOTON AXION CONVERSION UNDER A STATIC MAGNETIC FIELD

is a bonafide record of the project work done by **Mr. Shahad Hussain K S** (Student ID DU2019MSC0067) at the Department of Physics, School of Fundamental & Applied Sciences, Assam Don Bosco University, under the guidance of **Dr. Debajyoti Dutta**, in partial fulfillment of the requirements of the *PSPR6012: Project Work* of the M.Sc. (Physics) curriculum.

Director, SFAS

Dr. Monmoyuri Baruah

Place: ADBU, Tapesia

Date: July, 2021



Department of Physics
School of Fundamental & Applied
Sciences

Assam Don Bosco University
Tapesia, Sonapur – 782 402

EXAMINATION CERTIFICATE

This is to certify that **Shahad Hussain K S** bearing **DU2019MSC0067** of **Department of Physics** has carried out the Project Work in a manner satisfactory to warrant its acceptance and also defended it successfully.

I wish him all success in future endeavours.

Examiners:

1. External Examiner
2. Internal Examiner
3. Internal Examiner

DECLARATION

I, Shahad Hussain K S, hereby declare that this report of the project work entitled “**Photon Axion Conversion Under A Static Magnetic Field**” is the record of the work carried out by me under the supervision of DR. DEBAJYOTI DUTTA, Assam Don Bosco University. The content of this project did not form the basis for the award of any previous degree to me or to the best of my knowledge to anybody else. I also declare that the project has not been submitted by me for any research degree in any other university or institute.

This is being submitted to the ASSAM DON BOSCO UNIVERSITY for the degree of Master of Science in Physics.

Shahad Hussain K S

Place: ADBU, Tapesia

Department of Physics

Date: July, 2021

Assam Don Bosco University

Tapesia – 782 402, Assam

India

ACKNOWLEDGEMENT

This project would not have been possible without the support of many people. Many thanks to my adviser, Dr. Debajyoti Dutta, who took the initiative to push me through the hectic work and helped make some sense of the confusion. Also thanks to my teachers, Dr. Samrat Dey, Dr. Ngangom Aomoa , and Dr. Faizuddin Ahmed, who offered guidance and support.

Thanks to the Assam Don Bosco University for providing me with the oppurtunity to complete this project. And finally, thanks to my parents, loved ones and numerous friends who endured this long process with me, always offering support and love.

Shahad Hussain K S

July, 2021

Department of Physics

Assam Don Bosco University.

ABSTRACT

In spite of the fact that it was predicted more than four decades ago, the axion is still the most convincing answer to the strong-CP problem and a well-motivated dark matter candidate, sparking a variety of elegant and ultra sensitive experiments based on axion–photon mixing. This article examines the first occurrences of non-one-dimensional scattering and derives enhanced probability for a specific model. We selected to characterise the inhomogenous magnetic field surrounding the solenoids axis by fitting a Gaussian distribution around its centre and calculating the three-dimensional axion conversion cross section from photon scattering for this particular scenario. An analysis and simulation in Python were performed on the correlation between the transmitted axion cross section and arbitrary variables. Furthermore, we talk about the different approaches that have been suggested to look for dark matter and solar axions. As a result of their application and development, the concept of an invisible axion has come under considerable pressure. These findings compel us to take a closer look at how experiments intended to discover axions are carried out, and to understand how to use this research on a large scale to understand the concepts of Dark matter detection.

KEY WORDS: Axion; primakoff effect; Photon–axion conversion; ; strong-CP problem; Dark matter;

Contents

1	INTRODUCTION	1
1.1	STRONG CP PROBLEM	1
1.1.1	θ_{QCD} and Neutron dipole moment	2
1.1.2	The PQ solution	3
2	AXION - A DARK MATTER CANDIDATE	5
2.1	AXION and DARK MATTER	5
2.2	AXION MODELS	8
2.2.1	Electromagnetic coupling	9
2.3	COSMOLOGICAL AXION PRODUCTION	10
2.3.1	Axion dark matter properties	10
2.3.2	Topological production of axions	10
2.3.3	Vaccum realignment method	12
3	PHOTON AXION CONVERSION IN A MAGNETIC FIELD	13
3.1	INTRODUCTION	13
3.2	LAGRANGIAN AND EQUATIONS OF MOTION	15
3.3	GREENS FUNCTION CALCULATION	17
3.3.1	Asymptotic limit of the wave function	19
4	CROSS SECTION CALCULATION WITH DIFFERENT MAGNETIC FIELD	21

4.1	FINITE SIZED SOLENOIDAL GENERATED POTENTIALS	21
4.1.1	Gaussian Distributed Magnetic Field	21
5	EXPERIMENTAL SEARCHES FOR DARK MATTER AXIONS	28
5.1	AXIONIC DARK MATTER	28
5.2	AXION HELIOSCOPES	31
5.2.1	Pioneering Axion Helioscope	32
5.2.2	The Tokyo Axion Helioscope (Sumico)	33
5.2.3	CERN Axion Solar Telescope (CAST)	33
5.2.4	Orbiting X-ray Telescopes	34
5.3	AXION MICROCAVITY EXPERIMENT	35
5.3.1	Early experiments	37
5.3.2	ADMX- Axion Dark Matter eXperiment	38
5.3.3	Future of Microwave Cavity Experiments	43
6	SUMMARY & CONCLUSION	45
	Bibliography	47
	Appendix A Python Plots and Codes	56
A.1	3D plots	56
A.1.1	σ_{tot} vs B vs R plot	56
A.1.2	σ_{tot} vs K vs R plot	60
A.1.3	σ_{tot} vs K vs B plot	64
A.2	2D plots	68

A.2.1	σ_{tot} vs K plot	68
A.2.2	σ_{tot} vs R plot	70
Appendix B Acronyms and Abbreviations		72

CHAPTER 1

INTRODUCTION

Contents

1.1	STRONG CP PROBLEM	1
1.1.1	θ_{QCD} and Neutron dipole moment	2
1.1.2	The PQ solution	3

1.1 STRONG CP PROBLEM

The Standard Model (SM) of elementary particles rose to prominence in the 1970s as the most accurate representation of all fundamental interactions other than gravity. It has since proven to be extremely successful, explaining virtually all important data with only a few parameters. However, it was recognised early on as a puzzle: one would not anticipate the strong interactions within the SM to retain parity P or the product CP of charge conjugation C with parity.

P and CP are observed to be conserved by strong interactions and electromagnetic interactions. On the other hand, weak interactions violate P, C, and CP. The problem with the SM is that unless an unforeseen cancellation occurs, the P and CP violation of the weak interactions causes P and CP violation in the strong interactions. The Strong CP Problem is what this is known as.

1.1. STRONG CP PROBLEM

1.1.1 θ_{QCD} and Neutron dipole moment

A parameter, θ_{QCD} , which appears as the coefficient of a P and CP odd term in the action density, controls the amount of P and CP violation in strong interactions.

$$\mathcal{L}_{\text{SM}} = \dots + \theta_{\text{QCD}} \frac{g_s^2}{32\pi^2} G_{\mu\nu}^a \tilde{G}^{a\mu\nu} \quad (1.1)$$

where the $G_{\mu\nu}^a$, $a = 1, 2, \dots, 8$, are the Quantum Chromodynamics (QCD) field strengths (QCD), $\tilde{G}^{a\mu\nu} \equiv \frac{1}{2}\epsilon^{\mu\nu\alpha\beta}G_{\alpha\beta}^a$, and g_s is the QCD coupling constant. We use units with $\hbar = c = 1$ and conventions with the Minkowski metric $(\eta_{\mu\nu}) = \text{diag}(+1, -1, -1, -1)$ and $\epsilon^{0123} = +1$ unless otherwise stated. All other terms in the SM action density, i.e. the terms that contribute to its various achievements, are shown by the dots. Eq. (1.1) shows the one term that is not a success. θ_{QCD} is an angle, i.e. it is cyclic with period 2π . QCD depends on θ_{QCD} because of the existence in that theory of quantum tunneling events, called "instantons", which violate P and CP if θ_{QCD} differs from zero or π . Since in actuality the strong interactions obey P and CP, as well as can be observed, θ_{QCD} must be approaching one of the CP conserving values. The experimental upper limit on the neutron electric dipole moment provides the best constraint: $|d_n| < 3 \cdot 10^{-26} \text{ e cm}$ (90% CL). For small θ_{QCD} the contribution of the term shown in Eq. (1.1) to the neutron electric dipole moment is of order

$$d_n \sim \theta_{\text{QCD}} \frac{m_u m_d}{m_u + m_d} \frac{1}{\Lambda_{\text{QCD}}} \frac{e}{m_n} \sim 3 \cdot 10^{-16} \theta_{\text{QCD}} \text{ e cm} \quad (1.2)$$

where m_u and m_d are the up and down quark masses, m_n is the neutron mass, and Λ_{QCD} is the QCD scale. θ_{QCD} should therefore be less than of order $10^{-10} \text{ (mod } \pi)$. $\theta_{\text{QCD}} = 0$ or π is unexpected in the SM because P and CP are violated by the weak interactions. CP violation is introduced by giving apparently random phases to the Yukawa couplings that give rise to the quark masses. The total phase of the quark mass matrix flows into θ_{QCD} , which is of order one in general. The Strong CP Problem is the puzzle of why θ_{QCD} , which should have been of order one, is less than 10^{-10} .

1.1. STRONG CP PROBLEM

1.1.2 The PQ solution

Peccei and Quinn (PQ) proposed a modification of the SM that provides a solution soon after the Strong CP Problem was identified. They postulated a $U_{PQ}(1)$ symmetry that

- 1) has the classical action's exact symmetry,
- 2) is spontaneously broken, and
- 3) has a colour anomaly

i.e. it is explicitly broken by the non-perturbative QCD instanton effects that make physics depend on the value of θ_{QCD} . When this recipe is followed, the axion decay constant is substituted by $\phi(x)/f_\phi$, $\phi(x)$ with $x = (x^0, x^1, x^2, x^3)$ is a dynamical pseudo-scalar field and f_ϕ is a quantity with is an energy-dimensioned quantity. The vacuum expectation value of order f_ϕ spontaneously breaches $U_{PQ}(1)$ symmetry. The associated Nambu-Goldstone boson is $\phi(x)$. The non-perturbative instanton effects that make physics rely on θ_{QCD} introduce an effective potential for $\phi(x)$, according to Weinberg and Wilczek (WW). The minimum of this effective potential was later shown to be at $\phi(x)$. The Strong CP problem is solved after the $\phi(x)$ field settles there.

The PQ mechanism alters the SM's low-energy effective theory by introducing a light pseudo-scalar particle known as the "axion," which is the quantum of the $\phi(x)$ field. The Axion's properties are largely determined by the value of the axion decay constant f_ϕ . The axion mass m_ϕ is inversely proportional to f_ϕ , as are all of its interaction strengths. f_ϕ is of order the electroweak scale in the original PQWW model, implying an axion that is relatively strongly coupled and heavy, i.e. m_ϕ of order 100 keV. Several laboratory experiments, including unsuccessful searches for axions in beam dumps and rare particle decays such as $K^+ \rightarrow \pi^+ + a$, as well as stellar evolution constraints, quickly ruled out the PQWW model. The latter is due to the fact that stars emit weakly coupled axions from their cores but only photons from their surfaces. If axions exist, stars have an additional mechanism for losing energy, causing them to evolve more quickly. Axion models with $f_\phi \lesssim 10^9$ GeV are ruled out when the negative results from accelerator-based axion searches are combined with stellar evolution constraints.

The original PQWW model is unworkable, yet the underlying idea of Peccei-Quinn symmetry and its accompanying axion is still valid today. $U_{PQ}(1)$ does not need to be

1.1. STRONG CP PROBLEM

broken at the electroweak scale, according to Jihn E. Kim and colleagues. It could be broken at any energy level, such as the hypothetical "grand unification scale" of 10^{15} GeV. When f_ϕ is large enough, the axion is exceedingly light and very weakly coupled ($m_\phi \simeq 6 \cdot 10^{-9}$ eV for $f_\phi = 10^{15}$ GeV) : all axion production and interaction rates are suppressed by about 25 orders of magnitude compared to the PQWW axion. The "Invisible axion" was created by arbitrarily increasing f_ϕ , a solution to the Strong CP Problem that elegantly avoids the limits imposed by laboratory searches and evolution of star.

Thankfully, cosmology saved the day. Indeed, axion field oscillations must begin sufficiently early in the history of the cosmos for $\phi(x)$ to relax to zero. Since the oscillation period is $2/m_\phi$, the axion must be suitably heavy. Because of the universe's finite age, there is a limit to how small m_ϕ , or equivalently how large f_ϕ , can be.

CHAPTER 2

AXION - A DARK MATTER CANDIDATE

Contents

2.1	AXION and DARK MATTER	5
2.2	AXION MODELS	8
2.2.1	Electromagnetic coupling	9
2.3	COSMOLOGICAL AXION PRODUCTION	10
2.3.1	Axion dark matter properties	10
2.3.2	Topological production of axions	10
2.3.3	Vaccum realignment method	12

2.1 AXION and DARK MATTER

Several cosmological parameters have been measured with high accuracy recently, and the results have shown an universe of which only a small portion can be viewed directly. Deuterium abundances anticipated by the hypothesis of big bang nucleosynthesis (BBN) have been measured, and it has been shown that baryonic matter accounts for just 4% of the total energy density of the universe . According to evidence gathered from the cosmic microwave background, along with supernovae searches, galaxy surveys and other measurements, the great bulk of the universe is composed of gravitational "Dark Matter" (26 %) and negative pressure "Dark Energy" (70 %).

The presence of "Dark Energy" has just recently been demonstrated (mainly by cosmic supernovae surveys conducted in the last decade), although the existence of "Dark Matter" has been known since the early 1930 s. That is when Fritz Zwicky observed that the member galaxies of the Coma cluster were moving much too fast to be gravi-

2.1. AXION and DARK MATTER

tationally bound by the bright matter, which led to the discovery of the Coma cluster itself. The two possibilities are that they were unbound, which would indicate that the cluster should have split apart billions of years ago, or that there was a significant quantity of undetected "dark matter" holding the system together. Because of these early discoveries, evidence for dark matter has been accumulating on sizes ranging from the size of dwarf galaxies (kiloparsecs) to that of the whole visible universe (gigaparsecs).

At this time, the best dark matter possibilities appear to be unknown non-baryonic particles that were left over after the big bang, according to current research. In terms of interactions with standard-model particles such as baryons, leptons, and photons, they would be considered to have only the weakest interactions. In light of recent research into the creation of cosmic structures, it appears that the vast majority of dark matter is "cold," that is, non-relativistic, at the time of galaxy formation's inception. Relativistic dark matter would likely to stream out of early density disturbances since it is collisionless, essentially smoothing out the cosmos before galaxies had a chance to form. The galaxies that we view now are typically surrounded by enormous halos of dark matter that stretch far beyond than their luminous limits, a phenomenon known as haloing. Dark matter density near the solar system is estimated to be about $\rho_{CDM} \approx 0.45 \text{ GeV cm}^{-3}$ based on measurements of the Milky Way's rotation curves (together with other observables such as microlensing surveys).

There are two main types of dark matter candidates: the general class of Weakly Interacting Massive Particles (WIMPs), which includes the supersymmetric neutralino as an example, and the axion, which was predicted as a solution to the so-called "Strong CP" problem but has not yet been seen. Despite the fact that both particles have strong motivations, this explanation will concentrate solely on the axion. Axion is a light chargeless pseudo-scalar boson (negative parity, spin-zero particle) predicted by the violation of the PQ symmetry, which is explained in detail in Chapter 1. In the late 1970s, this symmetry was first proposed as a way to explain why charge (C) and parity (P) appear to be preserved in strong interactions, despite the fact that the QCD Lagrangian contains an overtly CP-violating component. Although this CP-violating term should have resulted in a readily observable electric dipole moment in the neutron, no such moment has been found to extremely high precision in any of the neutron's experiments.

The spontaneous symmetry breaking (SSB) scale of the Peccei-Quinn symmetry f_ϕ ,

2.1. AXION and DARK MATTER

is the essential parameter dictating most of the axion's features. The mass and axion coupling are both inversely proportional to f_ϕ , with the mass specified as

$$m_\phi \simeq 6.3 \text{ eV} \left(\frac{10^{12} \text{ GeV}}{f_\phi} \right) \quad (2.1)$$

and the axion photon coupling constant ($g_{\phi\gamma\gamma}$) expressed as

$$g_{\phi\gamma\gamma} \equiv \frac{\alpha}{2\pi f_\phi} C \quad (2.2)$$

where C is a dimensionless model dependent coupling parameter and α is the fine structure constant. In general, C is assumed to be ~ 0.97 for the KSVZ (Kim-Shifman-Vainshtein-Zakharov) class of axions and ~ -0.36 for the more pessimistic grand-unification-theory inspired DFSZ (Dine-Fischler-Srednicki-Zhitnitskii) models. Because interactions are proportional to the square of the couplings, these C values tend to limit the feasible axion-to-photon conversion rates to a few orders of magnitude at any given mass.

Initially, f_ϕ was thought to be on the electroweak scale ($f_\phi \sim 250 \text{ GeV}$), implying an axion mass of order 100 KeV and strong couplings visible in accelerators .

Searches for axions in particle and nuclear experiments, together with astrophysics limitations, quickly dropped its possible mass to $m_\phi \leq 3 \times 10^{-3} \text{ eV}$, equating to $f_\phi \geq 10^9 \text{ GeV}$.

These low-mass axions were first assumed to be undetectable since their couplings are inversely proportional to f_ϕ . They were dubbed "invisible" axions.

It was discovered that a general lower limit on the axion mass may also be derived from cosmology. Axions would be abundant at the moment of the big bang, thanks to several mechanisms which is discussed in this paper. The overall contributions to the universe's energy density from axions formed using the vacuum misalignment approach may thus be written as

$$\Omega_\phi \sim \left(\frac{5\mu\text{eV}}{m_\phi} \right)^{7/6} \quad (2.3)$$

This implies that the axion mass is $m_\phi \geq 10^{-6} \text{ eV}$ (any lighter and the axions would

2.2. AXION MODELS

overclose the universe, $\Omega_\phi \geq 1$). When the astrophysical and experimental constraints are added together, the axion has a mass range of $\mu\text{eV} - \text{meV}$, with the lower values being more likely if the axion is the primary component of dark matter. The axions produced in the early cosmos around the QCD phase transition, when the axion mass switches on, would have momenta. The temperature of the surrounding plasma was $T \simeq 1 \text{ GeV}$, while the temperature of the surrounding plasma was $\sim 10^{-8} \text{ eV} c^{-1}$. Furthermore, because such axions are so weakly coupled, they will never be in thermal equilibrium with anything else. This means they'd be non-relativistic "cold" dark matter right away, and they'd be able to build structures around density perturbations rather soon.

A massive halo of particles travelling at relative velocities of the order of $10^{-3} c$ would make up the axion dark matter in the galaxy today. It's unknown if any or all of the axions would be gravitationally thermalized, but they'd have to be going slower than the local escape velocity of $2 \times 10^{-3} c$ to be bound in the galaxy. Non-thermalized axions may still be oscillating into and out of the galaxy's gravitational well. These axions would have extremely small velocity dispersions (on the order of $10^{-17} c$), and the variances in velocity from different infalls (first time falling into the galaxy, first time flying out, second time falling in, etc.) would be correlated with the galaxy's development.

2.2 AXION MODELS

Axion models known as 'Invisible Axion Models' because of their extremely weak couplings are still possible. The PQ symmetry is decoupled from the electroweak scale in an invisible axion model, and it spontaneously breaks at a considerably higher temperature, lowering the axion mass and coupling strength. The KSVZ and DFSZ models are two benchmark, invisible axion models. Both of these theories produce an axion with permissible mass and couplings.

The standard Higgs doublet is the only Higgs doublet in the KSVZ model. An additional electroweak singlet scalar field introduces the axion as its phase. The known quarks cannot couple directly to such a field because this would result in unacceptably large quark masses. Instead, the scalar is connected to another heavy quark, this time

2.2. AXION MODELS

an electroweak singlet. The interactions of the heavy quark with the other fields then induce the axion couplings.

The DFSZ model, like the PQWW model, has two Higgs doublets and an additional electroweak singlet scalar. At the PQ symmetry-breaking scale, it is the electroweak singlet that acquires a vacuum expectation value. The scalar couples to quarks and leptons through interactions with the two Higgs doublets, rather than directly.

String compactifications produce PQ symmetries, which are always broken by an instanton. While this might seem to make the axion an excellent dark matter candidate, string models favour a PQ scale considerably higher than what cosmology allows, provides an assessment on the current scenario. It is difficult to lower the PQ scale below $1.1 \times 10^{16} \text{ GeV}$, as mentioned in 'Axions in string theory' by Svrcek and Witten, while it is much easier to raise its value.

2.2.1 Electromagnetic coupling

Axion couplings to other particles are inversely proportional to f_ϕ in general, but the exact strength of these couplings varies depending on the model. The coupling between axions and photons, for example, can be represented as

$$\mathcal{L}_{\phi\gamma\gamma} = g_{\phi\gamma\gamma} \phi \mathbf{E} \cdot \mathbf{B} \quad (2.4)$$

\mathbf{E} and \mathbf{B} are the components of the electromagnetic field. The coupling constant is

$$g_{\phi\gamma\gamma} = \frac{g_\gamma \alpha}{\pi f_\phi} \quad (2.5)$$

where g_γ is a constant containing the model dependence, $10^9 \text{ GeV} \lesssim f_\phi \lesssim 10^{12} \text{ GeV}$ is the axion decay constant, of the order of the PQ scale. Explicitly,

$$g_\gamma = \frac{1}{2} \left(\frac{E}{N} - \frac{2(4+z)}{3(1+z)} \right) \quad (2.6)$$

where z is the mass ratio of the up and down quarks, N is the axion colour anomaly, and E is the axion electromagnetic anomaly. The phrase holding the mass ratios of light quarks has a value of 1.95. E/N is the ratio that causes model dependence. E and

2.3. COSMOLOGICAL AXION PRODUCTION

N are connected in grandunifiable models, and $E/N = 8/3$. This is where the DFSZ axion model comes in, with $g_\gamma = 0.36$ in this example. $E = 0$ and $g_\gamma = 0.97$ for a KSVZ axion.

The development of the KSVZ and DFSZ axion models demonstrates that an axion can address the strong CP problem. While significant in terms of itself, the axion also offers an intriguing possibility for the universe's cold dark matter.

2.3 COSMOLOGICAL AXION PRODUCTION

2.3.1 Axion dark matter properties

Axions meet both of the requirements for cold dark matter: (i) a non-relativistic population of axions could exist in sufficient quantities in our universe to provide the required dark matter energy density, and (ii) they are effectively collisionless, with gravitational interactions being the only significant long-range interactions.

$$m_\phi \simeq 6 \times 10^{-6} \text{eV} \left(\frac{10^{12} \text{ GeV}}{f_\phi} \right) \quad (2.7)$$

Axion dark matter is non-relativistic, despite its small mass, since cold populations are formed out of balance. Cold axions are created by three mechanisms: vacuum realignment, string decay, and domain wall decay. The history of the axion field as the cosmos expands and cools is discussed in this section to see how and when axions are formed. We also go over vacuum realignment production in brief, note here that this mechanism will always contribute to cold axion populations, and it may be the sole one, as mentioned below.

2.3.2 Topological production of axions

There are two crucial scales in the generation of dark matter axions. The first is the temperature at which the PQ symmetry breaks, denoted by the symbol T_{PQ} . Which of the three methods contributes the most to the cold axion population is determined by whether this temperature is higher or lower than the inflationary reheating tem-

2.3. COSMOLOGICAL AXION PRODUCTION

perature, T_R . The second scale is the temperature at which the axion mass becomes important due to non-perturbative QCD effects. The QCD effects are insignificant at high temperatures, and the axion mass is negligible. At a critical point, t_1 , when $m_\phi t_1 \sim 1$, the axion mass becomes essential. $T_1 \simeq 1$ GeV is the temperature of the cosmos at t_1 .

At early dates and temperatures larger than T_{PQ} , the PQ symmetry remains unbroken. It spontaneously breaks at T_{PQ} , and the axion field, proportionate to the phase of the complex scalar field obtaining a vacuum expectation value, can have any value. The phase changes continuously from one horizon to the next, altering by order one. Axion strings emerge as topological flaws.

If $T_{PQ} > T_R$, the axion field is homogenised over enormous distances and the string density is diminished by inflation to the point where our visible universe is exceedingly unlikely to contain any axion strings. The axion field is not homogenised in the scenario $T_{PQ} < T_R$, and strings radiate cold, massless axions until non-perturbative QCD effects become substantial at temperature, T_1 .

There is no agreement on the expected spectrum of axions from string radiation, and there are two options. Strings either fluctuate several times before entirely decaying and axion production is sharply peaked around a dominant mode, or much faster decay occurs, generating a spectrum inversely proportional to momentum. Rapid decay generates approximately 70 times less axions than slow string decay, resulting in distinct cosmic constraints on axion mass.

The axion strings become the limits of N domain walls as the cosmos cools to T_1 . When $N = 1$, the walls quickly emit cold axions and disintegrate (domain wall decay). Because the vacuum is multiply degenerate and there is at least one domain wall per horizon if $N > 1$, the domain wall problem occurs. These walls will eventually dominate the energy density, causing the cosmos to expand as $S \propto t^2$, where S denotes the scale factor. Although different solutions to the domain wall problem have been presented by S. Chang, C. Hagmann, and P. Sikivie (Phys. Rev., D59:023505, 1999). we will assume $N = 1$ or $T_{PQ} > T_R$ in this case.

As a result, if $T_{PQ} < T_R$, string and wall degradation contribute to axion energy density. If $T_{PQ} < T_R$ and the axion string density is diluted by inflation, these methods have no meaningful contribution to the density of cold axions. Then, only vacuum realignment

2.3. COSMOLOGICAL AXION PRODUCTION

will make a major contribution.

2.3.3 Vacuum realignment method

Cold axions will be created independently of T_R via vacuum realignment. The details of this method are out of scope of this paper, but the basic mechanism is as follows. The axion field amplitude at T_{PQ} can be any magnitude. If $T_{PQ} > T_R$, inflation will cause homogeneity, and the axion field will be single valued over our observable universe. Non-perturbative QCD effects generate an axion field potential. When these effects become significant, the axion field's potential begins to oscillate. As non relativistic matter, these oscillations do not decay and add to the local energy density. Thus, independent of the inflationary reheating temperature, vacuum realignment produces a cold axion population.

(for further study, please see the article: arXiv:1904.05707 [astro-ph.CO])

CHAPTER 3

PHOTON AXION CONVERSION IN A MAGNETIC FIELD

Contents

3.1	INTRODUCTION	13
3.2	LAGRANGIAN AND EQUATIONS OF MOTION	15
3.3	GREENS FUNCTION CALCULATION	17
3.3.1	Asymptotic limit of the wave function	19

3.1 INTRODUCTION

Low-mass axions were once assumed to be "invisible" to typical observational technologies because to their extremely slow decay rates and weak interactions with hadronic matter and electromagnetism. Sikivie, on the other hand, demonstrated that the inverse Primakoff effect substantially accelerates the decomposition of dark matter axions under a strong static magnetic field.

One photon is "replaced" by a virtual photon in a static magnetic field, while the other maintains the axion's energy, which is equal to the rest-mass energy ($m_\phi c^2$) plus the nonrelativistic kinetic energy. In Eq. (2.4), \mathbf{B} is essentially converted to \mathbf{B}_0 , the static magnetic field. As B_0^2 , the axion's decay rate effectively increases. The Feynman diagrams of the axion photon interaction for the two scenarios are shown in Figure 3.1.

Sikivie presented a method for detecting axion dark matter based on the Primakoff effect, in which a microwave cavity permeated by a strong magnetic field is utilised to resonantly increase the number of photons produced by axion decay. When the resonant frequency $f \approx \frac{m_\phi c^2}{h}$, where h is Planck's constant, the axion-photon conversion

3.1. INTRODUCTION

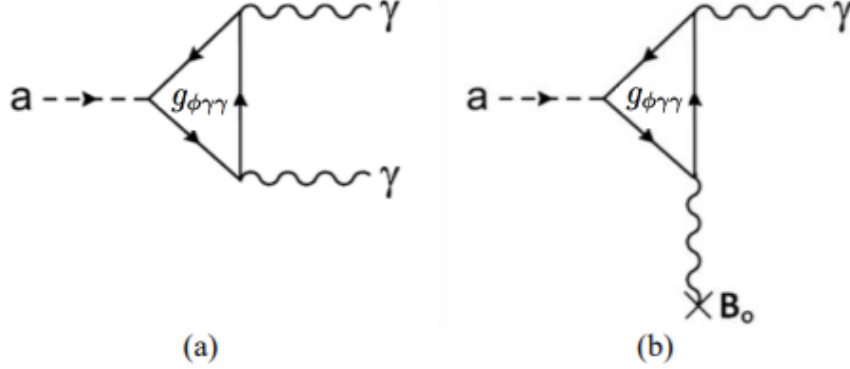


Figure 3.1 Axion decay into photons as illustrated by Feynman diagram . a) The vacuum conversion. b) In a static magnetic field, the inverse Primakoff effect

is enhanced. There is also a slight correction owing to the axion's kinetic energy, but it is negligible for cold dark matter ($\frac{\Delta E}{E} \approx 10^{-6}$). This axion dark matter detector is known as a haloscope, according to Sikivie.

The two-photon coupling of axions or axion-like particles allows for transitions between them and photons in external electric or magnetic fields as shown in Fig.3.1. This mechanism serves as the basis for the experimental searches for galactic dark matter axions and solar axions . The astrophysical implications of this mechanism have also been widely investigated and reviewed . The phenomenological consequences of an extremely light or massless axion would be particularly interesting in several astrophysical circumstances such as polarization of radio-galaxies and quasars, the diffuse X-ray background, or ultra-high energy cosmic rays.

One fascinating cosmological consequence of this technique is photonaxion conversion induced by intergalactic magnetic fields, which results in the dimming of distant light sources, particularly type Ia supernovae, which are employed as cosmic distance indicators. SNe Ia at redshifts of $0.3 \lesssim z \lesssim 1.7$ appear fainter than expected from the luminosity-redshift relation in a decelerating Universe, a finding usually interpreted as evidence for acceleration of the cosmic expansion rate and thus for a cosmic equation of state (EoS) dominated by a cosmological constant.

A slowly changing scalar field, or something more stranger. The darkening generated by photon-axion conversion could imitate this phenomenon, offering an alternate explanation to cosmic acceleration. Although it still required some non-standard fluid to account for the Universe's flatness, this model appeared capable of explaining the

3.2. LAGRANGIAN AND EQUATIONS OF MOTION

SN-dimming via a fundamentally different mechanism.

However, if light from distant SNe Ia is partially transformed to axion-like particles and reaches us, the same mechanism would apply to all remote sources of electromagnetic radiation. As a result, it appears important to update the many arguments constraining photon-axion conversion in intergalactic magnetic fields, particularly the limitations originating from cosmic microwave background (CMB) spectral distortions and quasar (QSO) spectral dispersion.

3.2 LAGRANGIAN AND EQUATIONS OF MOTION

This chapter examines the conversion of axions to photons in the lack of cavities or reflecting walls for the photons in a static magnetic field.

In this paper we will consider a system described by the action for the axion and electromagnetic fields:

$$S = \int d^4x \left[-\frac{1}{4} F^{\mu\nu} F_{\mu\nu} - \frac{1}{2} (\partial_\mu \phi \partial^\mu \phi + m^2 \phi^2) + \frac{g}{4} \phi F^{\mu\nu} \tilde{F}_{\mu\nu} \right] \quad (3.1)$$

with

$$\tilde{F}_{\mu\nu} = \frac{1}{2} \epsilon^{\mu\nu\alpha\beta} F_{\alpha\beta} \quad (3.2)$$

where ϕ is a real scalar field representing the axion, $F_{\mu\nu}$ is the electromagnetic field tensor, and g is the coupling constant.

We are interested in the physical condition of photons and axions propagating in the presence of a static magnetic field as a background. We will assume that this magnetic background B is dependent on r and points in any direction denoted by \hat{n} , such that the important part of the interaction term is

$$\int d^4x \beta \phi E_{\hat{n}} \quad (3.3)$$

3.2. LAGRANGIAN AND EQUATIONS OF MOTION

where $\beta = gB(\vec{r})$ and $E_{\hat{n}}$ is the component of the photon electric field parallel to the background magnetic field

Using the Coulomb gauge and ignoring photon field components that do not couple to the axion via the magnetic field, (3.1) becomes

$$S = -\frac{1}{2} \int d^4x [\partial_\mu A \partial^\mu A + (\partial_\mu \phi \partial^\mu \phi + m^2 \phi^2) - 2\beta \phi \partial_t A] \quad (3.4)$$

where A is a magnetic vector potential. Choosing the temporal gauge $A_0 = 0$, then the relevant electric field component becomes $E_{\hat{n}} = \partial_t A$

$$(\partial_\mu \partial^\mu + m^2) \phi(\vec{r}, t) = \beta(\vec{r}) \partial_t A(\vec{r}, t) \quad (3.5)$$

$$(\partial_\mu \partial^\mu) A(\vec{r}, t) = -\beta(r) \partial_t \phi(\vec{r}, t) \quad (3.6)$$

where $\mu = (0, 1, 2, 3)$ Now considering the scenario of an incident wave with time dependency $f(\vec{r})e^{i\omega t}$, where $f(\vec{r})$ represents the fields $\phi(\vec{r}, t)$ or $A(\vec{r}, t)$. In free space regions where the magnetic field vanishes (zones I, III of figure 1) the $f(\vec{r})$ for A is $e^{\pm i\vec{k}_p \cdot \vec{r}}$ and for ϕ is $e^{\pm i\vec{k}_a \cdot \vec{r}}$, where \vec{k}_p is photon wave vector, \vec{k}_a is axion wave vector.

We write the fields as follows after performing a perturbation expansion in powers of β .

$$\phi(\vec{r}, t) = \phi^{(0)}(\vec{r}, t) + \phi^{(1)}(\vec{r}, t) + \dots \quad (3.7)$$

$$A(\vec{r}, t) = A^{(0)}(\vec{r}, t) + A^{(1)}(\vec{r}, t) + \dots \quad (3.8)$$

where the equations of motion (3.5) and (3.6) becomes

$$(\partial_\mu \partial^\mu + m^2) \phi^{(0)}(\vec{r}, t) = 0 \quad (3.9)$$

$$(\partial_\mu \partial^\mu) A^{(0)}(\vec{r}, t) = 0 \quad (3.10)$$

$$(\partial_\mu \partial^\mu + m^2) \phi^{(1)}(\vec{r}, t) = \beta(\vec{r}) \partial_t A^{(0)}(\vec{r}, t) \quad (3.11)$$

3.3. GREENS FUNCTION CALCULATION

$$(\partial_\mu \partial^\mu) A^{(1)}(\vec{r}, t) = -\beta(\vec{r}) \partial_t \phi^{(0)}(\vec{r}, t) \quad (3.12)$$

In the equations (3.11) and (3.12), we can see that the solutions of the unperturbed fields (3.9) and (3.10) becomes the sources for the perturbed fields.

3.3 GREENS FUNCTION CALCULATION

Calculating the solution for the equation (3.11) using Greens's function method, and we are interested in the solutions for $G_m(\vec{r}, t)$

$$(\partial_\mu \partial^\mu + m^2) G_m(\vec{r}, t) = -\delta^3(\vec{r}) \delta(t) \quad (3.13)$$

A direct calculation in fourier space gives us the desired Green's function, where $\tilde{G}_m(r, t) = \frac{1}{k^2 - m^2}$, writing $k^2 - m^2 = \omega^2 - \omega_k^2$

$$G_m(\vec{r}, t) = \frac{1}{(2\pi)^4} \int d^3k \frac{e^{i(\vec{k} \cdot \vec{r} - \omega t)}}{\omega^2 - \omega_k^2} \quad (3.14)$$

with $\omega_k = \sqrt{k^2 + m^2}$.

In order to deal with the singularities in carrying out the ω integration, we will treat ω as a complex number and treat the integration as a contour integral running along the real ω axis. The singularities on the contour are avoided by pushing the singularities at $\omega = \omega_k$ infinitesimally away from the real axis. Since we want the retarded Green's function solution, that is $G_m(r, t) = 0$ for $t = 0$. we integrate on the real ω axis, with poles $\pm \omega_k$ shifted to $\pm \omega_k - i\epsilon$. When $t < 0$, closing the contour up gives 0; when $t > 0$, closing the contour down gives the retarded Green function

$$G_m^R(\vec{r}, t) = -\theta(t) \frac{1}{(2\pi)^3} \int \frac{d^3k}{\omega_k} e^{i\vec{k} \cdot \vec{r}} \sin(\omega_k t) \quad (3.15)$$

For our case of incident photons from the left, we take the incident photon field as a monochromatic wave $A^{(0)} = e^{i(\vec{k}_p \cdot \vec{r} - \omega t)}$ and $\phi^{(0)} = 0$,

3.3. GREENS FUNCTION CALCULATION

so that the inhomogeneous equation (3.11) reads

$$(\partial_\mu \partial^\mu + m^2) \phi^{(1)}(\vec{r}, t) = -i\bar{\omega} \beta(\vec{r}) e^{i(\vec{k}_p \cdot \vec{r} - \bar{\omega} t)} \quad (3.16)$$

then particular solution construction using the Green's function for the equation (3.11) will be given by

$$\phi^{(1)}(\vec{r}, t) = -i\bar{\omega} \int d^3r' dt' G(\vec{r} - \vec{r}', t - t') \beta(\vec{r}') e^{i(\vec{k}_p \cdot \vec{r}' - \bar{\omega} t')} \quad (3.17)$$

$$= -i\bar{\omega} \int_V d^3r' \beta(\vec{r}') e^{i\vec{k}_p \cdot \vec{r}'} \int_{-\infty}^{\infty} dt' G_m^R(\vec{r} - \vec{r}', t - t') e^{-i\bar{\omega} t'} \quad (3.18)$$

where we have assumed $\beta(\vec{r}) = 0$ outside the interval 0 to L. Substituting the Retarded green's function (3.15) in the above equation we get

$$= -i\bar{\omega} \int_V d^3r' \beta(\vec{r}') e^{i\vec{k}_p \cdot \vec{r}'} \int_{-\infty}^{\infty} dt' -\theta(t - t') \frac{1}{(2\pi)^3} \times \int_{-\infty}^{\infty} \frac{d^3k}{\omega_k} e^{i\vec{k} \cdot (\vec{r} - \vec{r}')} \sin \omega_k(t - t') e^{-i\bar{\omega} t'} \quad (3.19)$$

$$= -i\bar{\omega} e^{-i\bar{\omega} t} \int_V d^3r' \beta(\vec{r}') e^{i\vec{k}_p \cdot \vec{r}'} \int_{-\infty}^{\infty} \frac{-1}{(2\pi)^3} \frac{d^3k}{\omega_k} e^{i\vec{k} \cdot (\vec{r} - \vec{r}')} \times \int_{-\infty}^{\infty} dt' \theta(t - t') e^{i\bar{\omega}(t - t')} \sin \omega_k(t - t') \quad (3.20)$$

the integral over t' can be done by substituting $T = t - t'$, there are only contrubutions from $T > 0$ because of the $\theta(T)$. after doing the integral on t' the equation (3.20) becomes,

$$= -i\bar{\omega} e^{-i\bar{\omega} t} \int_V d^3r' \beta(\vec{r}') e^{i\vec{k}_p \cdot \vec{r}'} \int_{-\infty}^{\infty} \frac{-1}{(2\pi)^3} \frac{d^3k}{\omega_k} e^{i\vec{k} \cdot (\vec{r} - \vec{r}')} \times \frac{\omega_k}{\omega_k^2 - \bar{\omega}^2} \quad (3.21)$$

writing $|\vec{r} - \vec{r}'| = R$ and now solving for the volume integral over k , the above equation becomes

$$= i\bar{\omega} e^{-i\bar{\omega} t} \int_V d^3r' \beta(\vec{r}') e^{i\vec{k}_p \cdot \vec{r}'} \times \frac{1}{(2\pi)^2} \int_0^\infty \frac{k^2 dk}{\omega_k^2 - \bar{\omega}^2} \int_{-1}^1 e^{ikR \cos \theta} d\cos \theta \quad (3.22)$$

3.3. GREENS FUNCTION CALCULATION

$$= i\bar{\omega}e^{-i\bar{\omega}t} \int_V d^3r' \beta(\vec{r}') e^{i\vec{k}_p \cdot \vec{r}'} \times \frac{2}{(2\pi)^2} \frac{1}{R} \int_0^\infty \frac{k \sin(kR)}{\omega_k^2 - \bar{\omega}^2} dk \quad (3.23)$$

solving separately for the integral over k after substituting $\omega_k^2 = k^2 + m^2$

$$\int_0^\infty \frac{k \sin(kR)}{k^2 + m^2 - \bar{\omega}^2} dk \quad (3.24)$$

The integral on k can be performed as usual in the complex plane by closing the contour in Upper Half plane for $r - r' > 0$ and for $r - r' < 0$ we close the contour in the Lower Half Plane, which gives the results,

$$\int_0^\infty \frac{k \sin(kR)}{(k + \sqrt{\bar{\omega}^2 - m^2})(k - \sqrt{\bar{\omega}^2 - m^2})} dk = \begin{cases} \frac{\pi}{2i} e^{+i\sqrt{\bar{\omega}^2 - m^2} R} ; & r - r' > 0 \\ \frac{\pi}{2i} e^{-i\sqrt{\bar{\omega}^2 - m^2} R} ; & r - r' < 0 \end{cases} \quad (3.25)$$

substituting the result (3.25) in to equation (3.23) thus we get the perturbed first order transmitted and reflected wave function.

$$\phi_{transmitted}^{(1)}(\vec{r}, t) = \frac{\bar{\omega}}{4\pi} e^{-i\bar{\omega}t} \int_V d^3r' \theta(r - r') \beta(\vec{r}') e^{i\vec{k}_p \cdot \vec{r}'} \left(\frac{e^{i\sqrt{\bar{\omega}^2 - m^2}(\vec{r} - \vec{r}')}}{|\vec{r} - \vec{r}'|} \right) \quad (3.26)$$

$$\phi_{reflected}^{(1)}(\vec{r}, t) = \frac{\bar{\omega}}{4\pi} e^{-i\bar{\omega}t} \int_V d^3r' \theta(r' - r) \beta(\vec{r}') e^{i\vec{k}_p \cdot \vec{r}'} \left(\frac{e^{-i\sqrt{\bar{\omega}^2 - m^2}(\vec{r} - \vec{r}')}}{|\vec{r} - \vec{r}'|} \right) \quad (3.27)$$

3.3.1 Asymptotic limit of the wave function

We will now demonstrate that for high values of r , the expression (3.26) will now be reduced. For ease of calculation we will substitute $\kappa = \sqrt{\bar{\omega}^2 - m^2}$. In a scattering experiment, because the detector is located at distances (away from the target) that are significantly greater than the size of the target (Figure 3.1), we have $r \gg r'$,

3.3. GREENS FUNCTION CALCULATION

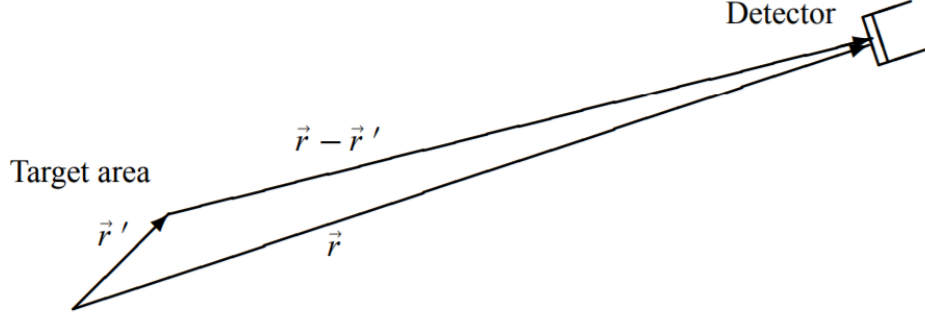


Figure 3.1. The distance r between the target and the detector is too large in comparison to the target's size r' . i.e : $r \gg r'$

Image courtesy : Zettili, Nouredine. Quantum Mechanics: Concepts and Applications. Chichester, U.K: Wiley, 2009. Print.

where r represents the distance from the target to the detector and r' represents the size of the detector (see Figure 3.1). If $r \gg r'$, we can approximate $\kappa |\vec{r} - \vec{r}'|$ and $|\vec{r} - \vec{r}'|^{-1}$ by

$$\kappa |\vec{r} - \vec{r}'| = k \sqrt{\vec{r}^2 - 2\vec{r} \cdot \vec{r}' + \vec{r}'^2} \simeq \kappa r - \kappa \frac{\vec{r}}{r} \cdot \vec{r}' = \kappa r - \vec{\kappa} \cdot \vec{r}' \quad (3.28)$$

$$\frac{1}{|\vec{r} - \vec{r}'|} = \frac{1}{r} \frac{1}{|1 - \frac{\vec{r} \cdot \vec{r}'}{r^2}|} \simeq \frac{1}{r} \left(1 + \frac{\vec{r} \cdot \vec{r}'}{r^2} \right) \simeq \frac{1}{r} \quad (3.29)$$

substituting (3.28) and (3.29) into the equations (3.26) and (3.27) and simplifying, we arrive at the equations for $\phi_{\text{reflected}}^{(1)}(\vec{r}, t)$ and $\phi_{\text{transmitted}}^{(1)}(\vec{r}, t)$,

$$\phi_{\text{transmitted}}^{(1)}(r, t) = \frac{e^{i(\kappa r - \bar{\omega} t)}}{r} \left[\frac{\bar{\omega}}{4\pi} \int_V d^3r' \theta(r - r') \beta(\vec{r}') e^{i(\vec{k}_p - \vec{\kappa}) \cdot \vec{r}'} \right] \quad (3.30)$$

$$\phi_{\text{reflected}}^{(1)}(r, t) = \frac{e^{-i(\kappa r + \bar{\omega} t)}}{r} \left[\frac{\bar{\omega}}{4\pi} \int_V d^3r' \theta(r' - r) \beta(\vec{r}') e^{i(\vec{k}_p + \vec{\kappa}) \cdot \vec{r}'} \right] \quad (3.31)$$

CHAPTER 4

CROSS SECTION CALCULATION WITH DIFFERENT MAGNETIC FIELD

Contents

4.1 FINITE SIZED SOLENOIDAL GENERATED POTENTIALS	21
4.1.1 Gaussian Distributed Magnetic Field	21

4.1 **FINITE SIZED SOLENOIDAL GENERATED POTENTIALS**

4.1.1 **Gaussian Distributed Magnetic Field**

We want to be able to acquire quantifiable values that can be used in a laboratory experiment, therefore we must explore a more realistic function to describe the magnetic field created by the solenoid in order to achieve this. As an initial model, we chose to characterise the inhomogeneous magnetic field around the solenoid's axis using a Gaussian distribution around its centre.

$$\vec{B}(r) = B_0 e^{\frac{-r^2}{R^2}} \hat{z} \quad (4.1)$$

From equation (3.30) , the scattering amplitude $f(\theta, \phi)$ of the transmitted wave function $\phi_{transmitted}^{(1)}(r, t)$ is given by

$$f(\theta, \phi) = \frac{\bar{\omega}}{4\pi} \int_V d^3r' \theta(r' - r) \beta(\vec{r}') e^{i(\vec{k}_p + \vec{k}) \cdot \vec{r}'} \quad (4.2)$$

4.1. FINITE SIZED SOLENOIDAL GENERATED POTENTIALS

where for simplification we substitute $\vec{q} = \vec{k}_p + \vec{\kappa}$ and $\beta(\vec{r}') = g B(\vec{r}')$. Where $\vec{B}(\vec{r}') = B_0 e^{-\frac{r'^2}{R^2}}$, then our above equation becomes

$$f(\theta, \phi) = \frac{\bar{\omega}}{4\pi} \int_V d^3r' \theta(r - r') g B_0 e^{-\frac{r'^2}{R^2}} e^{i\vec{q} \cdot \vec{r}'} \quad (4.3)$$

Evaluating the volume integral using cylindrical coordinates

$$\Rightarrow \frac{\bar{\omega}}{4\pi} g B_0 \int_0^\infty e^{-\frac{r'^2}{R^2}} r' dr' \int_0^{2\pi} d\phi e^{iqr' \cos \phi} \int_0^L dz \quad (4.4)$$

$$= \frac{\bar{\omega}L}{4\pi} g B_0 \int_0^\infty e^{-\frac{r'^2}{R^2}} r' dr' \int_0^{2\pi} d\phi e^{iqr' \cos \phi} \quad (4.5)$$

Using the integral definition for Bessel function of First Kind

$J_0(qr') = \int_0^{2\pi} d\phi e^{iqr' \cos \phi}$ we have

$$\Rightarrow \frac{\bar{\omega}L}{2} g B_0 \int_0^\infty e^{-\frac{r'^2}{R^2}} r' dr' J_0(qr') \quad (4.6)$$

$$= g B_0 \frac{\bar{\omega}L}{2} \times \frac{R^2}{2} e^{-\frac{q^2 R^2}{4}} \quad (4.7)$$

Therefore our scattering amplitude

$$f(\theta, \phi) = \frac{\bar{\omega}L}{4} g B_0 R^2 e^{-\frac{q^2 R^2}{4}} \quad (4.8)$$

where the explicit dependence of q on the scattering angle θ is given by

$$q^2 = 2K^2(1 - \cos \theta) = 4K^2 \sin^2(\theta/2) \quad (4.9)$$

where $K = k_p$ which is the incident photon momentum. The differential cross section is related to the scattering amplitude:

$$\frac{d\sigma}{d\Omega}(\theta, \phi) = |f(\theta, \phi)|^2 \quad (4.10)$$

4.1. FINITE SIZED SOLENOIDAL GENERATED POTENTIALS

The probability density for detecting the scattered projectile at a given angle is the straightforward interpretation.

Therefore the differential cross section is

$$\frac{d\sigma}{d\Omega}(\theta, \phi) = \left(\frac{\bar{\omega}L}{4} g B_0 R^2 \right)^2 \times e^{-\frac{q^2 R^2}{2}} \quad (4.11)$$

Integrating the differential cross section $\frac{d\sigma}{d\Omega}$ across the complete solid angle (4π steradians) yields the total cross section σ :

$$\sigma_{tot} = \oint_{4\pi} \frac{d\sigma}{d\Omega} d\Omega = \int_0^{2\pi} \int_0^\pi \frac{d\sigma}{d\Omega} \sin \theta d\theta d\varphi \quad (4.12)$$

Finding Total cross section from equation (4.11)

$$\sigma_{tot} = \int_0^{2\pi} \int_0^\pi \left(\frac{\bar{\omega}L}{4} g B_0 R^2 \right)^2 e^{-\frac{q^2 R^2}{2}} \sin \theta d\theta d\varphi \quad (4.13)$$

Using (4.9) in (4.13)

$$\Rightarrow 2\pi \left(\frac{\bar{\omega}L}{4} g B_0 R^2 \right)^2 \int_0^\pi e^{-K^2 R^2 (1-\cos\theta)} \sin \theta d\theta \quad (4.14)$$

$$= 2\pi \left(\frac{\bar{\omega}L}{4} g B_0 R^2 \right)^2 e^{-K^2 R^2} \times \int_0^\pi e^{K^2 R^2 \cos\theta} \sin \theta d\theta \quad (4.15)$$

Using the integral definition of modified bessel function (4.15) becomes

$$\Rightarrow 2\pi \left(\frac{\bar{\omega}L}{4} g B_0 R^2 \right)^2 e^{-K^2 R^2} \times \frac{KR}{\sqrt{2\pi}} I_{\frac{1}{2}}((KR)^2) \quad (4.16)$$

Therefore we arrive at the expression for Total cross section

$$\sigma_{tot} = \sqrt{2\pi} \left(\frac{\bar{\omega}L}{4} g B_0 R^2 \right)^2 KR e^{-(KR)^2} I_{\frac{1}{2}}((KR)^2) \quad (4.17)$$

where B_0 is the magnetic field strength of the solenoid, K is the incident photon momentum $\bar{\omega}$ is the frequency of the incident beam, L is the length of the solenoid and

4.1. FINITE SIZED SOLENOIDAL GENERATED POTENTIALS

R is the radius of the solenoid.

The Axion transmission probability P_{trans} can be found dividing σ_{tot} by the lateral surface area of the solenoid of length L , and radius R

$$P_{trans} = \frac{\sigma_{tot}}{2\pi RL} \quad (4.18)$$

The QCD inspired axions with masses up to the ~ 1 eV range are our core motivation. We use the value of the coupling constant g from the CAST collaboration's latest result to determine the magnitude of the entire cross-section. Following the coherent inverse Primakoff-effect, CAST is looking for axions formed in the sun and travelling to Earth by trying to detect photons from the conversion of axions inside a continuous magnetic field. CAST has set an upper bound on the magnitude of the axion-photon coupling constant of $g_{\phi\gamma\gamma} \lesssim 2.2 \times 10^{-10} \text{ GeV}^{-1}$ for an axion mass of $m_\phi \lesssim 0.4$ eV, in collaboration with the Japanese axion helioscope Sumico . The (Axion Like Particles)

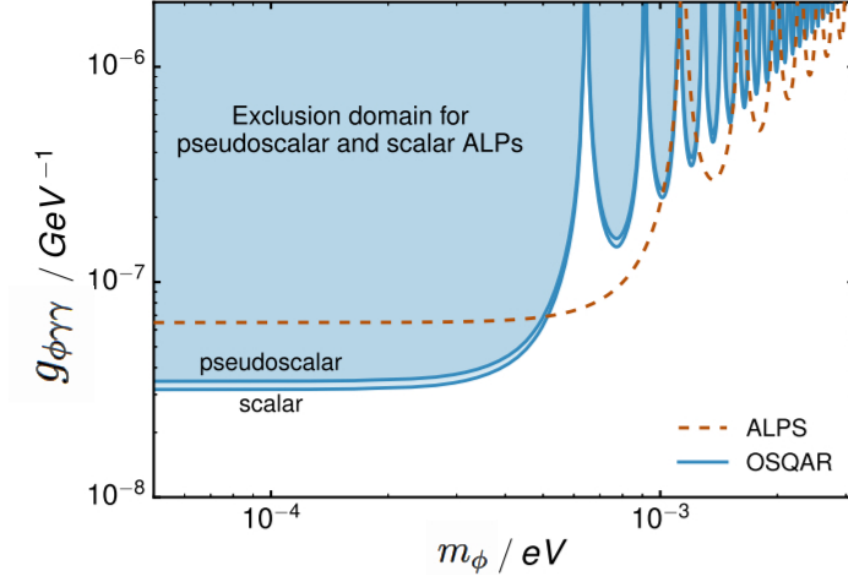


Figure 4.1. Exclusion limits for PS-ALP and S-ALP searches obtained in vacuum by the current OSQAR LSW experiment at 95% C.L.

ALPS Collaboration's exclusion limitations are also shown in Fig. 6, which summarises (Pseudo-Scalar-ALP) PS-ALPs and (Scalar-ALPs) S-ALPs searches. For the pseudo scalar and scalar searches for $m_\phi < 2 \times 10^{-4}$ eV, a limit for the diphoton couplings of $g_{\phi\gamma\gamma} < 3.5 \times 10^{-8} \text{ GeV}^{-1}$ and $g_{\phi\gamma\gamma} < 3.2 \times 10^{-8} \text{ GeV}^{-1}$ is found. These findings

4.1. FINITE SIZED SOLENOIDAL GENERATED POTENTIALS

impose the most restrictive limits on ALP searches in the almost massless limit that LSW experiments have yielded so far. Throughout this work, we will utilise the value $g = g_{\phi\gamma\gamma} = 0.88 \times 10^{-10} \text{ GeV}^{-1}$. Multiplying the 3D scattering cross section σ_{tot} with the incident photon flux F gives the number of events per second N_{tot} . A few examples for the transmitted Axion conversion Probability, Cross section and Number of events are below in the Tables 4.1(a), (b), (c)

B [Tesla]	R [cm]	σ_{tot} [barn]	N_{tot} [sec ⁻¹]	P_{trans}
10	1	2.699×10^{-7}	9.906×10^{-15}	4.296×10^{-35}
10	10	2.830×10^{-3}	1.039×10^{-10}	4.504×10^{-32}
6	2	1.630×10^{-6}	5.982×10^{-14}	1.297×10^{-34}
6	20	1.630×10^{-2}	5.982×10^{-10}	1.297×10^{-31}

4.1(a) : For X-ray Photons ($E = 124 \text{ eV}$)

B [Tesla]	R [cm]	σ_{tot} [barn]	N_{tot} [sec ⁻¹]	P_{trans}
10	1	3.073×10^{-14}	1.128×10^{-21}	4.891×10^{-42}
10	10	2.987×10^{-8}	1.096×10^{-15}	4.754×10^{-37}
6	2	7.075×10^{-13}	2.596×10^{-20}	5.630×10^{-41}
6	20	6.324×10^{-8}	2.321×10^{-14}	5.032×10^{-36}

4.1(b) : For Visible light ($E = 1.7 \text{ eV}$)

B [Tesla]	R [cm]	σ_{tot} [barn]	N_{tot} [sec ⁻¹]	P_{trans}
10	1	8.702×10^{-27}	3.194×10^{-34}	1.385×10^{-54}
10	10	8.702×10^{-21}	3.194×10^{-28}	1.385×10^{-49}
6	2	2.005×10^{-25}	7.358×10^{-33}	1.596×10^{-53}
6	20	2.005×10^{-19}	7.358×10^{-27}	1.596×10^{-48}

4.1(c) : For Microwave Photon ($E = 1.24 \text{ meV}$)

Table 4.1(a), (b), (c) : Total cross-section, number of events, and axion-photon conversion probability for various magnetic field strength (B), solenoid Radius (R) and

4.1. FINITE SIZED SOLENOIDAL GENERATED POTENTIALS

solenoid Length (L) = 10 cm values, as well as for $g = 0.88 \times 10^{-10} \text{ GeV}^{-1}$. The magnetic field units were converted from Tesla to eV^2 using rationalised natural units, with the conversion being $1 \text{ T} = 195 \text{ eV}^2$. (please see appendix A in [63] for more details).

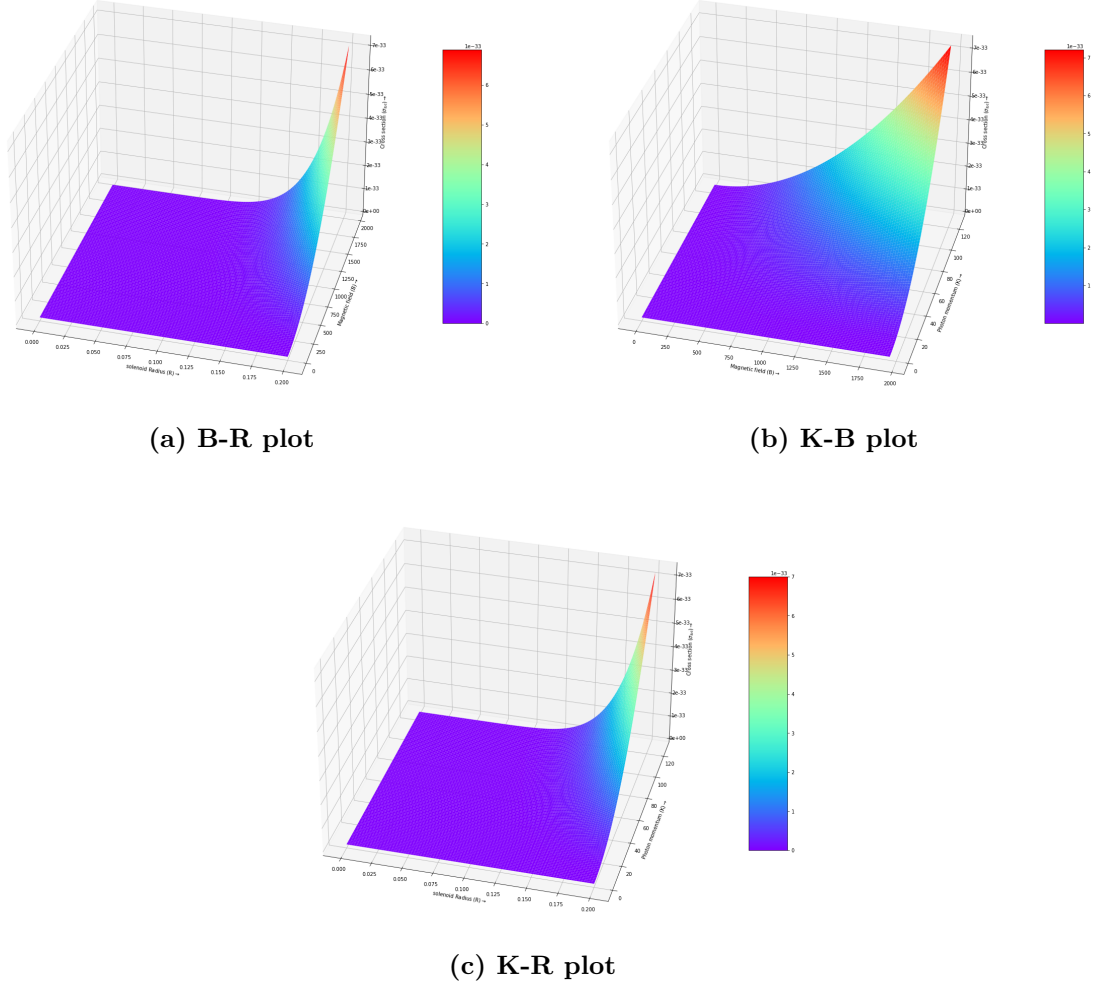


Figure 4.2 : Visualizing the behaviour of the total cross section σ_{tot} with respect to arbitrary B, R, and K values
(3D plot using matplotlib library in python - see Appendix A for the detailed Graphs and Python codes)

We can see from the above 3D graphs that the arguments of the Modified Bessel function $I_{\frac{1}{2}}((KR)^2)$ and the $e^{-(KR)^2}$ are K and R. The behaviour of the total cross section is heavily influenced by these two arbitrary variables. The increase in solenoid radius R from 0 to 20 cm blows up the axion cross section by a factor of 7. Similarly, the

4.1. FINITE SIZED SOLENOIDAL GENERATED POTENTIALS

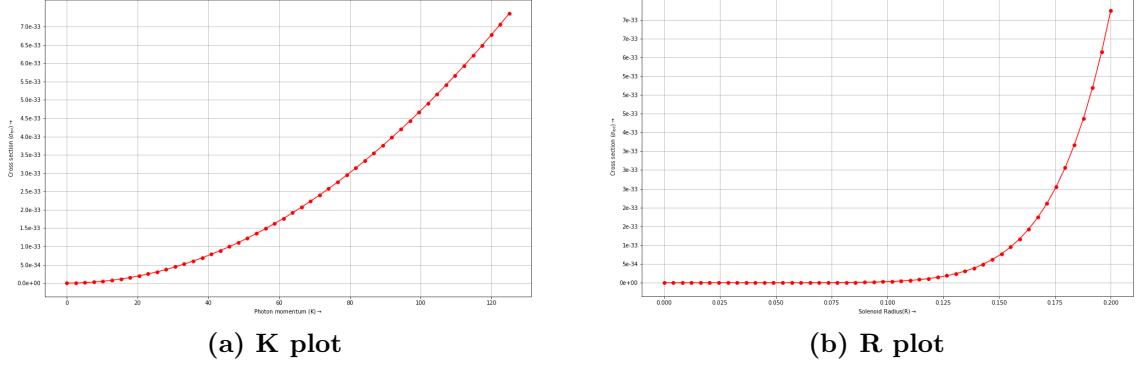


Figure 4.3 : Visualizing the behaviour of the total cross section σ_{tot} with respect to arbitrary B, R, and K values

similar pattern can be seen for the ranges of K and B.

As a result, we're going further into the equation (4.17), trying to figure out how the cross section and probability behave in relation to the variables K and R. In the absence of any change in R, we obtain the plot 4.3(a) by graphing the curve against the cross section. In the image, as one moves along the positive K axis, the slope steadily increases from 0 - 124 eV, indicating that with a constant solenoid radius, the rise in incident photon momentum accelerates the axion production rate represented by the increase in cross section. If we look at the slope of the R in figure 4.3 (b), we see that it is much larger than the slope of the K, which means that the increase in cross section with respect to an increase in solenoid radius is much greater than the increase in cross section with respect to incident photon momentum is relatively small.

When you look at the equation 4.17, you will notice that the arguments of the exponential function and the modified bessel function are both $(R * K)^2$, which results in a difference in the slope of the equation. As seen in figure 4.3(b), if we express frequency and momentum in energy units and simplify equation 4.17, we obtain the K^3 and R^5 terms, accordingly. The additional R^2 term contributes to the rise in the slope of the R vs σ_{tot} plot (figure 4.3(b)). If the solenoid's radius is increased tenfold, it will result in an increase in the cross section σ_{tot} on the order of eight times greater. When the incident photon momentum is ten times greater, the cross section σ_{tot} grows by an order of magnitude greater than two times. As a result, the slopes of the plots 4.3(a) and 4.3(b) deviate by such a wide margin from one another.

CHAPTER 5

EXPERIMENTAL SEARCHES FOR DARK MATTER AXIONS

Contents

5.1	AXIONIC DARK MATTER	28
5.2	AXION HELIOSCOPES	31
5.2.1	Pioneering Axion Helioscope	32
5.2.2	The Tokyo Axion Helioscope (Sumico)	33
5.2.3	CERN Axion Solar Telescope (CAST)	33
5.2.4	Orbiting X-ray Telescopes	34
5.3	AXION MICROCAVITY EXPERIMENT	35
5.3.1	Early experiments	37
5.3.2	ADMX- Axion Dark Matter eXperiment	38
5.3.3	Future of Microwave Cavity Experiments	43

5.1 AXIONIC DARK MATTER

Axions produced in the early universe with a mass ranging from μeV to meV could account for the cold dark-matter component of the universe, as described in the review by P. Sikivie on cosmological axions in Sect. 1.6, axions produced in the early universe with a mass ranging from μeV to meV could account for the cold dark-matter component of the universe axion detectors based on microwave resonant cavity studies are currently the most sensitive detectors for cold dark matter axions. The metallic conductor at the centre of such a device serves as a cavity for electromagnetic fields such as photons. It is possible to modify the resonant frequency of the magnetic-field permeated cavity such that it coincides with the frequency of the axion field by adjusting

5.1. AXIONIC DARK MATTER

the size of the magnetic-field permeated cavity (which is related to the axion mass). Excess cavity power output could be detected with sensitive microwave receivers in this circumstance because the axions will resonantly change into quasi-monochromatic photons. Figure 5.3 depicts a schematic representation of the working principle of this type of detector.

Axion distribution in the galactic halo would be represented by the width of the signal obtained, which would provide information not only about the axion mass but also about its distribution in the galactic halo. Furthermore, as illustrated in Fig. 5.3, the signal may possibly have finer substructure as a result of axions that have recently entered the galaxy and have not yet thermalized. The reader is directed to Sikivie’s review for a more extensive discussion of the axion distribution in the galactic halo, which is also included in this section.

Consequently, because the dark-matter axion has an extremely small mass range, the expected signal is miniscule, and as a result the sensitivity of the experiment is critically dependent on the quality of the microwave receivers used in the experiment (see Chap. 8 by Carosi and van Bibber). Small volume cavities ($\sim 1000 \text{ cm}^3$) and high frequency transistor amplifiers were used in two pioneering experiments carried out in the 1980s at Rochester-Brookhaven-Fermilab (RBF) and the University of Florida (UF), but their sensitivities fell short by two or three orders of magnitude of the sensitivity required to probe the theoretically motivated region in the axion parametric spherical symmetry.

In response to an increase in sensitivity, experiments such as ADMX were developed that are currently gathering data with a larger resonant cavity than the preceding studies, while still utilising the HFET amplifiers as previously described. The authors’ results are consistent with the absence of any axion signal, and they provide the best upper limits for the axion to photon coupling constant $g_{\phi\gamma\gamma}$ in the lowest mass range ($m_\phi \approx 10^{-4} - 10^{-6} \text{ eV}$). It is feasible to boost the sensitivity of ADMX even further by using a new amplifier technology based on Superconducting Quantum Interference Devices (SQUID), which is currently under development. This would allow researchers to probe the theoretically favored axion parameter range.

The CARRACK experiment in Kyoto is another example of a second-generation experiment. Although it similarly makes use of a resonant cavity to generate the axion-converted photons, the signal detection is carried out using a Rydberg-atom single-

5.1. AXIONIC DARK MATTER

quantum detector, which has extremely low noise photon counting capabilities due to its low noise. This experiment is still in the early stages of development.

A suitably light axion, whose density relative to the Universe’s critical density is given by,

$$\Omega_a \approx \left(\frac{6\mu\text{eV}}{m_\phi} \right)^{\frac{7}{6}} \quad (5.1)$$

is a promising dark matter candidate. The whole dark matter density of the Universe, $\Omega_m \approx 0.27$, would be accounted for by an axion of $m_\phi \approx 20 \mu\text{eV}$ (within a factor of nearly two). Much lighter axions would overclose the Universe if the initial misalignment angle was not tuned; hence, $m_\phi \approx 1 \mu\text{eV}$ may be regarded a strong lower limit on the axion mass m_ϕ . The relative contribution of axion creation via the vacuum realignment mechanism and radiation from topological flaws has been a source of debate (axion strings, domain walls). Although a definite answer is doubtful in the near future, the prevailing agreement is that the sum of all contributions to Ω_a might raise the axion mass corresponding to Ω_{DM} by two orders of magnitude. Because we’re mainly concerned in creating conservative ranges for experiments right now, searches should aim for the μeV scale. The formation of thermal axions in cosmology provides an upper bound on axion mass, the hot dark matter limit of around 1 eV, however we are not interested in this topic.

Axions are likewise subject to stringent restrictions as a result of stellar evolution. Axions with masses greater than $\sim 16 \text{ meV}$ would have quenched the SN1987a neutrino pulse, therefore constraining the axion mass from above.

Galactic globular clusters provide the best indirect stellar bound on the axion-photon coupling, $g_{\phi\gamma\gamma} < 0.66 \times 10^{-10} \text{GeV}^{-1}$. This bound just eclipsed the greatest direct stellar bound, $g_{\phi\gamma\gamma} \approx 0.88 \times 10^{-10} \text{GeV}^{-1}$, obtained by the CERN Axion Solar Telescope (CAST) hunt for solar axions. Such couplings for PQ axions correspond to masses well outside the open mass region (i.e., $10^{-6} \text{ eV} < m_\phi < 10^{-2} \text{ eV}$). A brief literature has recently indicated that the brightness function of white dwarfs (degenerate stars undergoing gravothermal cooling) may require an extra cooling process, which might be explained by axions in the $\sim 10 \text{ meV}$ range. The evidence is inconclusive; additionally, such masses are beginning to encroach on the SN1987a favored zone.

The open mass window for axions has long been thought to be in the $10^{-6} - 10^{-2} \text{ eV}$

5.2. AXION HELIOSCOPES

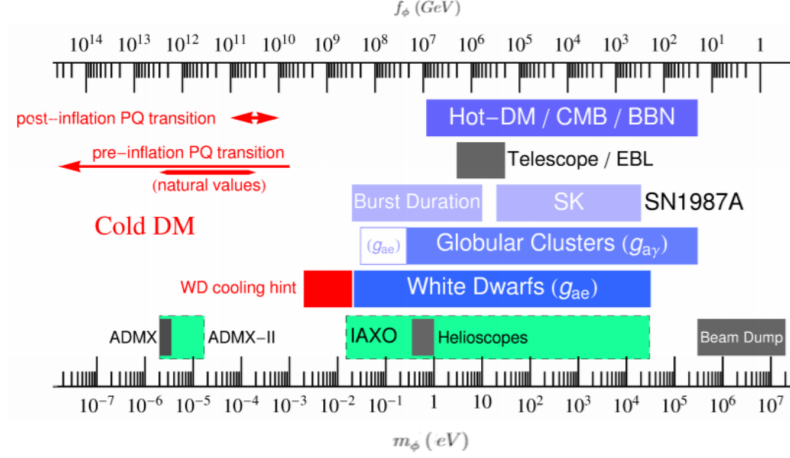


Figure 5.1. Ranges of exclusion as described in the text. The dark gaps represent the approximate CAST and ADMX search ranges, while the green sections represent the future upgrade’s intended reach. Using $z = 0.56$ and the KSVZ values for the coupling strengths, coupling strength limitations are translated into limits on m_ϕ and f_ϕ . For regular or modified axions, the "Beam Dump" bar is an approximate approximation of the exclusion range. The DFSZ model with an axion-electron coupling of $\cos^2 \beta = 1/2$ is used in the "Globular Clusters" and "White Dwarfs" ranges. The exclusion range for Cold Dark Matter is particularly ambiguous; ranges for pre-inflation and post-inflation Peccei-Quinn transitions are presented.

range. String theories, on the other hand, are abundant in axions or ALPs greater than 100 in any given realisation yet such theories naturally favour $f_\phi \approx 10^{15} - 10^{16}$ GeV, corresponding to neV scale masses. It’s impossible to identify which of them, if any, solves the strong-CP problem and which is cosmologically relevant.

5.2 AXION HELIOSCOPES

Axion helioscopes, or magnetic solar telescopes, are currently the most sensitive axion experiments in the mass range of $10^{-5} \text{eV} \lesssim m_\phi \lesssim 1 \text{eV}$. The underlying physical basis of such a telescope is represented in Fig. 5.2 and is based on an idea proposed by P. Sikivie in 1983. If axions are created in the Sun, they would arrive on Earth as a virtually parallel axion beam after about 500 s (the apparent diameter of the axion emission zone on the solar disc is $\approx 0.1^\circ$). The time reversed Primakoff effect, i.e., $a + \gamma_{\text{virtual}} \rightarrow \gamma$, is used to detect the axion on Earth, where the axion interacts with

5.2. AXION HELIOSCOPES

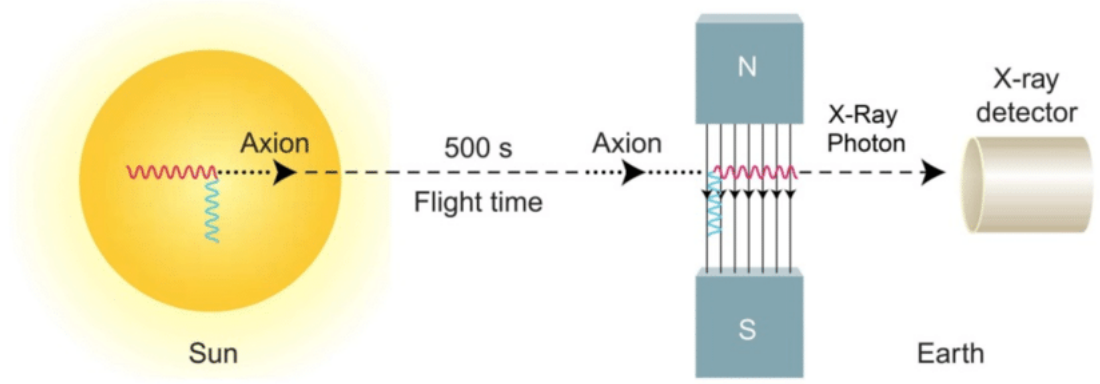


Figure 5.2: An axion helioscope's operation is based on the following concept. In a high magnetic field, axions generated in the Sun's core by the Primakoff effect would be transformed back into photons, completing the cycle. These photons, which have an energy spectrum that matches that of the arriving axions, may be captured by an X-ray detector located at the end of the magnet field area in due course.

a virtual photon provided by a transversal magnetic field and reconverts into a real photon. Because these "reconverted" photons have the same energy and momentum as the axion, their energy distribution is identical to the solar axion's energy spectrum. An X-ray detector on the magnetic field's end would gather photons and look for an axion signal above the detector's background. For the given differential solar axion spectrum, the estimated number of reconverted photons reaching the detector is

For the given differential solar axion spectrum, the estimated number of reconverted photons reaching the detector is.

$$N = \int \frac{d\Phi_a}{dE} P_{a \rightarrow \gamma} S t dE \quad (5.2)$$

The differential axion flux at the Earth is $d\Phi_a/dE$, the effective axion-sensitive magnetic aperture is S , the measurement period is t , and the conversion probability of an axion into a photon is $P_{a \rightarrow \gamma}$, the magnet is positioned in the same way as traditional telescopes, allowing it to monitor the Sun's path across the sky.

5.2.1 Pioneering Axion Helioscope

A 1.8 m long magnet driven by a 2.2 T transverse magnetic field was used to build the first axion helioscope in the early 1990s by the RBF collaboration. The photons from the axion-to-photon conversion were collected using a proportional counter running

5.2. AXION HELIOSCOPES

with a gas mixture of argon and methane (90% to 10%) as a detector. For a period of $\approx 15 \text{ min day}^{-1}$, the helioscope may be directed to the Sun. This configuration was used to investigate two distinct areas of the axion mass range (with and without a gas in the conversion volume), placing the following constraints on $g_{\phi\gamma\gamma}$ and m_ϕ

$$\begin{aligned} g_{\phi\gamma\gamma} &< 3.6 \times 10^{-9} \text{ GeV}^{-1} & \text{for } m_\phi < 0.03 \text{ eV} \\ g_{\phi\gamma\gamma} &< 7.7 \times 10^{-9} \text{ GeV}^{-1} & \text{for } 0.03 \text{ eV} < m_\phi < 0.11 \text{ eV} \end{aligned}$$

5.2.2 The Tokyo Axion Helioscope (Sumico)

In the late 1990s, Tokyo constructed a new helioscope with enhanced sensitivity (2.3 m). For this experiment, sixteen PIN photodiodes were employed as X-ray detectors, and the superconducting magnet was mounted on a polar mount, allowing the system to track the Sun in a declination range of -28° to $+28^\circ$ and a right ascension range of 360° . The Tokyo helioscope was able to watch the Sun for 24 h a day thanks to a superior tracking mechanism, and the Sun observation period was substantially enhanced. The Tokyo cooperation was able to employ roughly 50% of their instrument's duty cycle to follow the Sun, with the remainder of the time being used for background observations. The experiment was separated into two parts, similar to the original method of the first phase was completed in 1997 with an evacuated conversion zone, and the second phase was completed in 2000 with the magnet pipe filled with helium gas to increase the sensitive axion mass range. The top limits on $g_{\phi\gamma\gamma}$ derived from both data taking periods are

$$\begin{aligned} g_{\phi\gamma\gamma} &< 6 \times 10^{-10} \text{ GeV}^{-1} & \text{for } m_\phi < 0.03 \text{ eV} \\ g_{\phi\gamma\gamma} &< 6.8 - 10.9 \times 10^{-10} \text{ GeV}^{-1} & \text{for } m_\phi < 0.3 \text{ eV} \end{aligned}$$

5.2.3 CERN Axion Solar Telescope (CAST)

The CERN Axion Solar Telescope, the world's most sensitive axion helioscope, is now in operation at CERN (CAST). It was constructed in 2002 by refurbishing a 9.26 m long prototype of a LHC dipole magnet with dual apertures. A transverse dipole magnetic field is homogeneously interleaved between the two parallel pipes of the magnet, each with a bore area of $A = 14.5 \text{ cm}^2$. The highest magnetic field that this prototype

5.2. AXION HELIOSCOPES

magnet can produce is ≈ 9 T. During dawn and sunset, the magnet is positioned on an azimuthal movable platform that allows it to track the Sun for 1.5 h ($\pm 8^\circ$ in height and $\approx 100^\circ$ in azimuth). Three detectors are attached to the ends of the magnet pipes to detect axions: a gaseous detector with a novel MICROMEGAS readout, an X-ray telescope with a pn-CCD chip as focal plane detector to detect axions during sunrise, and a Time Projection Chamber (TPC) that covers the opposite end of the magnet pipes, ready to collect axions during sunset. During the years 2013 to 2015, CAST collected data with the conversion region removed. An upper limit on the axion to photon coupling constant has been determined in the absence of any axion signal.

$$g_{\phi\gamma\gamma} < 0.66 \times 10^{-10} \text{ GeV}^{-1} \quad \text{for } m_\phi < 0.02 \text{ eV}$$

at the 95% confidence level. This is the best laboratory limit a helioscope has ever attained. It encompasses a wide range of masses and outperforms the best astrophysical limit, which was determined from the development of horizontal-branch stars in globular clusters. The CAST experiment's design was updated in 2005, allowing it to proceed to the second phase of the experiment, when the magnet pipes are filled with ^4He or ^3He gas. CAST will be able to increase its sensitivity to a maximum axion mass of ≈ 1.1 eV in this setup.

5.2.4 Orbiting X-ray Telescopes

As with the axion helioscopes discussed above, the same operating concept applies to orbiting detectors sensitive to hard X-rays (for example, for the RHESSI solar X-ray observatory, which has a threshold greater than ~ 3 keV). Axion-to-photon conversion can occur either in the terrestrial magnetic field or in the magnetic field near the solar atmosphere, depending on the circumstances. Despite the significant disparities between the two methods, their sensitivity can compete with the finest earth-bound helioscope (see the next section), but only for axion rest masses in the range of $10^{-4}\text{eV}/c^2$ or less. According to the findings of this article, solar X-ray telescopes in space may be used as the most sensitive solar axion antennas for large axions ($m_\phi > 10^{-3} \text{ eV}/c^2$) by employing the solar magnetic fields near the photosphere in addition to the solar X-ray telescopes. One may be tempted to think of such a system as an indirect approach in axion helioscopy, which would be incorrect. When compared to direct axion-detection

5.3. AXION MICROCAVITY EXPERIMENT

approaches utilising axion helioscopes, the findings acquired in this manner can be just as significant, if not more so, and eventually have a higher built-in sensitivity.

Table 1. Axion helioscopes are being compared in terms of their figures of merit . When calculating the magnetic field strength, B equals the strength of the magnetic field, L equals the length, S equals the effective axion-sensitive magnetic aperture, and t is the tracking time per day (for the orbiting telescopes).

Helioscope	$(BL)^2$ T ² m ²	$(BL)^2 S$ T ² m ⁴	$(BL)^2 St$ T ² m ⁴ hours
RBF	16	$\sim 3 \times 10^{-2}$	$\sim 1 \times 10^{-2}$
Sumico	85	$\sim 10 \times 10^{-2}$	$\sim 120 \times 10^{-2}$
CAST	6946	2000×10^{-2}	6000×10^{-2}
In orbit	324	20000×10^{-2}	—

5.3 AXION MICROCAVITY EXPERIMENT

In the solar vicinity, the black halo of our Milky Way galaxy has a density of order 10^{-24} gr/cm³. The halo particles have v velocities in the $10^{-3}c$ range. We are surrounded by a pseudo-scalar field pulsating with angular frequency if the dark matter is axions:

$$\omega_a = E_a = m_\phi + \frac{1}{2}m_\phi v^2 = m_\phi (1 + \mathcal{O}(10^{-6})) \quad (5.3)$$

The axion electromagnetic interaction (4) becomes

$$\mathcal{L}_{a\gamma\gamma} = -g_\gamma \frac{\alpha}{\pi} \frac{1}{f_\phi} a \vec{E} \cdot \vec{B}_0 \quad (5.4)$$

in the presence of an externally supplied magnetic field \vec{B}_0 . As mentioned in the preceding section, it enables for the conversion of axions to photons and vice versa. It is advantageous to have the conversion process occur inside an electromagnetic cavity in the case of dark matter axions, assuming their mass is in the 10^{-6} to 10^{-4} eV range. When one of the cavity modes equals the axion signal's angular frequency, the cavity collects the photons produced and boosts the conversion process through resonance.

5.3. AXION MICROCAVITY EXPERIMENT

The conversion power from an optimised experiment is given by

$$\begin{aligned}
P_a &= g_{\phi\gamma\gamma}^2 V B_0^2 \varrho_a C_{lmn} \frac{1}{m_\phi} \min(Q_L, Q_a) \\
&= 0.5 \times 10^{-26} \text{ W} \left(\frac{V}{5001} \right) \left(\frac{B_0}{7 \text{ T}} \right)^2 C \left(\frac{g_\gamma}{0.36} \right)^2 \\
&\quad \times \left(\frac{\varrho_a}{0.5 \times 10^{-24} \text{ g cm}^{-3}} \right) \\
&\quad \times \left(\frac{m_\phi}{2\pi(\text{GHz})} \right) \min(Q_L, Q_a)
\end{aligned} \tag{5.5}$$

V denotes the cavity volume, B_0 denotes the magnetic field, Q_L denotes the cavity's loaded quality factor (defined as centre frequency over frequency bandwidth), $Q_a = 10^6$ denotes the quality factor of the axion signal (axion energy over spread in energy or $1/\beta^2$), ϱ_a denotes the axion mass density at the detection point (earth), where C_{lmn} is the form factor for one of the transverse magnetic cavity modes (TM_{lmn}). Essentially, this form factor is the normalised overlap integral of the external static magnetic field, $\mathbf{B}_0(\mathbf{x})$, and the oscillating electric field, $\mathbf{E}_\omega(\mathbf{x})e^{i\omega t}$, of that particular cavity mode. It can be determined with the use of

$$C = \frac{|\int_V d^3x \mathbf{E}_\omega \cdot \mathbf{B}_0|^2}{\mathbf{B}_0^2 V \int_V d^3x \epsilon |\mathbf{E}_\omega|^2} \tag{5.6}$$

in where ϵ denotes the dielectric constant of the cavity. The TM_{010} mode has the highest form factor ($C_{010} = 0.69[19]$) for a cylindrical cavity with a homogenous longitudinal magnetic field. Though Model-dependent, equation (5.5) can offer an idea of the exceedingly small signal expected from axion-photon conversions in a resonant cavity, measured in yoctowatts (10^{-24} W). This is far less than the 2.5×10^{-21} W of power received from the Pioneer 10 spacecraft's 7.5 W transmitter's last transmission in 2002, when it was 12.1 billion kilometres from Earth. Furthermore, because the experiment would require tuning orders of magnitude of frequency in short frequency steps, the Dicke radiometer equation governs how long one can integrate at each frequency to optimise signal-to-noise:

$$\frac{s}{n} \equiv \frac{P_s}{P_n} = \frac{P_s \sqrt{\Delta v t}}{k T_n} \tag{5.7}$$

The signal-to-noise ratio is s/n , the signal's bandwidth is Δv , the integration time is t , and the signal and noise powers are P_s and P_n , respectively. $T_n = T_{\text{phys}} + T_{\text{elec}}$.

5.3. AXION MICROCAVITY EXPERIMENT

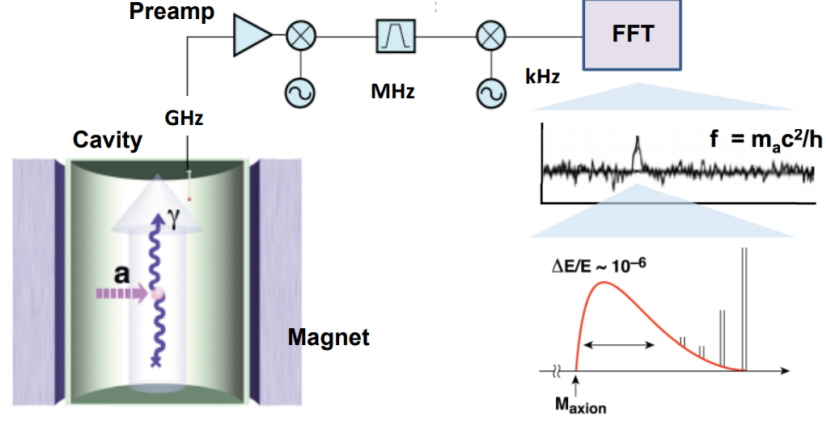


Figure 5.3. The microwave cavity search for dark-matter axions is depicted in this diagram. In a strong magnetic field, axions resonantly convert to a quasi-monochromatic microwave signal; the signal is collected from the cavity by an antenna, amplified, down converted, and the power spectrum estimated by an FFT. Any fine structure in the signal would provide crucial details about our galaxy’s formation.

ADMX recently completed a transition from conventional heterojunction field-effect transistors (HFETs or HEMTs) with a noise equivalent temperature of $T_{\text{elec}} \sim 2$ K, to superconducting quantum interference device (SQUID) amplifiers, whose noise equivalent noise temperatures can reach the quantum limit, $T_{\text{elec}} \sim 50\text{mK}$ at 750MHz when cooled to comparable physical temperature limit. This method will allow them to reach the DFSZ model axions and cross the open mass range considerably more quickly in the long run. Carosi describes his microwave cavity studies in this issue of Focus.

5.3.1 Early experiments

Soon after the experimental concept was published, two pilot initiatives in the $(1 - 4 \text{ GHz})$ range were launched at Brookhaven National Laboratory (BNL) and the University of Florida (UF). These used a few litre cavities and the greatest conventional amplifiers available at the time, such as HFET amplifiers. These amplifiers were not sensitive enough to reach PQ axions with noise temperatures in the $\sim 3 - 20\text{K}$ range. Nonetheless, these two experiments laid the groundwork for much of the design philosophy and knowledge regarding microwave cavities that is still used in today’s research.

5.3. AXION MICROCAVITY EXPERIMENT

In the history of microwave cavity experiments, the CARRACK experiment in Kyoto, Japan, was a watershed moment. The goal of CARRACK was to significantly lower the system noise temperature by lowering the physical temperature of the experiment to $\sim 15\text{mK}$ with a $^3\text{He} - ^4\text{He}$ dilution refrigerator and eliminating the amplifier noise contribution by using a Rydberg-atom single-quantum detector instead of a standard linear amplifier. The standard quantum limit (SQL) is an irreducible noise contribution that occurs in linear amplifiers: $kT_{\text{SQL}} = h\nu$. The Rydberg-atom single-quantum detector can be thought of as a tunable radio-frequency (RF) photomultiplier tube, with the photon interacting as a particle rather than a wave, avoiding the SQL. Tada et al. observed the cavity's blackbody photon spectrum as a function of temperature from 2.527 GHz to $T = 67\text{mK}$, about a factor of two lower than the SQL of $\sim 120\text{mK}$. CARRACK was a success from a technological standpoint, but it was eventually too complicated to be used as a production experiment.

5.3.2 ADMX- Axion Dark Matter eXperiment

The Axion Dark Matter eXperiment (ADMX) at Lawrence Livermore National Laboratory is seen in Fig. 8.1 as a schematic representation. It comprises of a cylindrical copper-plated steel cavity with two axial tuning rods that is housed within the cavity of the experiment. As a result, the resonant frequency may be perturbed by moving them transversely from the border of the hollow wall to its centre. The cavity itself is housed within the bore of a superconducting solenoid, which generates a powerful and continuous axial magnetic field around the cavity itself. In this case, a tiny adjustable antenna is used to link the cavity's electromagnetic field to the low-noise reception electronics. First, two cryogenic amplifiers with extremely low noise are connected in series to amplify the signal in this circuit. Using a room-temperature post-amplifier, the signal is then amplified once more before being sent to a double-heterodyne receiver. It comprises of an image reject mixer that reduces the signal frequency from the cavity resonance (hundreds of MHz – GHz) to an intermediate frequency (IF) of 10.7 MHz, which is then amplified. In order to reject noise power outside of a 35 kHz window centred on the IF, a crystal bandpass filter is utilised. Once this has been accomplished, the signal is blended down to practically audible frequencies (35 kHz) and examined by fast-Fourier transform (FFT) electrical circuitry. The FFT circuitry computes a 50 kHz bandwidth that is centred on 35 kHz. By adjusting the

5.3. AXION MICROCAVITY EXPERIMENT

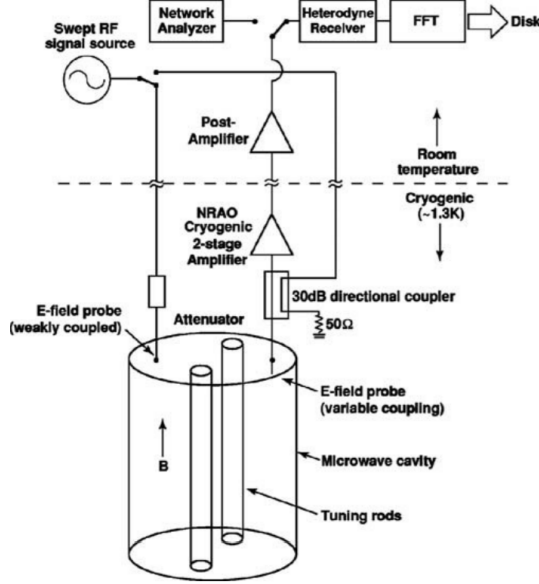


Figure 5.4. The ADMX experiment is depicted in a schematic design that includes both the resonant cavity (which is housed within the bore of a superconducting solenoid) and the receiver electronics chain.

tuning rods to produce a new resonant TM_{010} mode, data is collected about every 1 kHz. Some of these components will be discussed in further detail in the following sections.

The primary magnet for ADMX was created in such a way that the $B_0^2 V$ contribution to the signal power was maximised (Figure 5.5). In the end, it was concluded that a superconducting solenoid would be the most cost-effective option, and that its extraordinarily large inductance (535 Henry) would have the additional benefit of maintaining a very steady magnetic field. An open magnet bore in the cryostat (see Fig. 5.5) allows the experimental insert with the cavity and liquid helium (LHe) reservoir to be lowered into the 6t magnet coil. The magnet coil is housed in a 3.6 m tall cryostat (see Fig. 5.5) with an open magnet bore. During operations, the magnet itself is immersed in a 4.2 K LHe bath in order to maintain the superconductivity of the niobium-titanium windings on the magnet. For the most part, the magnet was held at a field strength of 7.6 T in the solenoid centre (with a drop to roughly 70% at the ends), although the experiment has recently been conducted at field strengths of up to 8.2 T. Because of the utilisation of cylindrical cavities in the ADMX experiment, it is possible to optimise the axion conversion volume in the solenoid bore. A copper-plated steel cylinder with

5.3. AXION MICROCAVITY EXPERIMENT

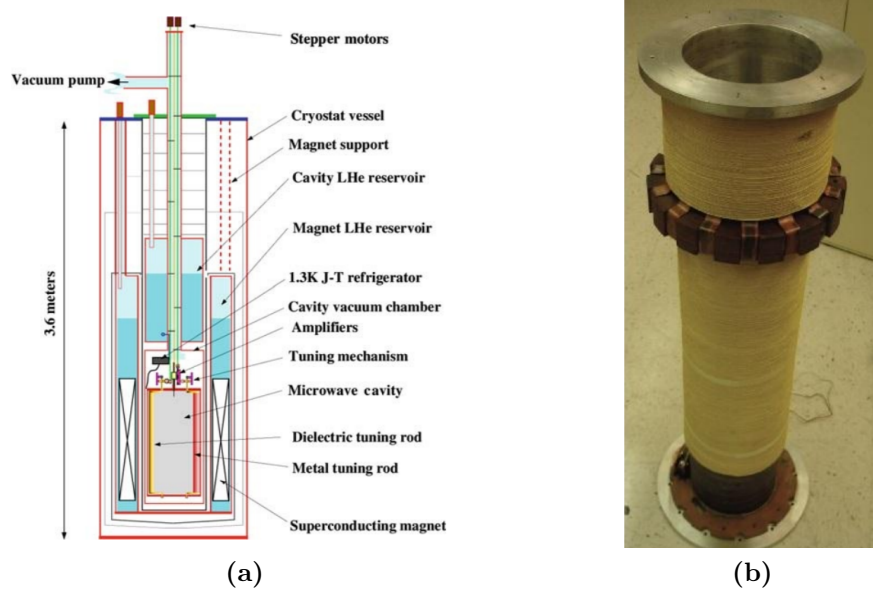


Figure 5.5 : (a) ADMX hardware overview, including the superconducting magnet and cavity insert (b) Superconducting solenoid “bucking” magnet.

sealed ends serves as the basis for these cylinders. The Helmholtz equation,

$$\nabla^2 \Phi + k^2 \Phi = 0 \quad (5.8)$$

where the wavenumber k is given by

$$k^2 = \mu \epsilon \omega^2 - \beta^2 \quad (5.9)$$

where β is the eigenvalue for the transverse (x, y) component, can be used to determine the electromagnetic field structure inside a cavity. The cavity modes are the standing wave solutions to (5.8). The boundary conditions of an empty cavity allow only transverse magnetic (TM) modes ($B_z = 0$) and transverse electric (TE) modes ($E_z = 0$). Three-dimensional standing waves are represented by the TM_{lmn} modes, where $l = 0, 1, 2, \dots$ is the number of azimuthal nodes, $m = 1, 2, 3, \dots$ is the number of radial nodes, and $n = 0, 1, 2, \dots$ is the number of axial nodes. The axions have the strongest coupling to the TM_{010} mode of the simplest structure.

By introducing metallic or dielectric tuning rods placed axially into the cavity, the resonance frequency of the TM_{010} mode may be changed. As you move closer to the centre, metallic rods boost the cavity resonant frequency, whereas dielectric rods reduce

5.3. AXION MICROCAVITY EXPERIMENT

it. These rods are connected to the ends of alumina arms of ADMX, which pivot around axles located in the upper and lower end plates (Fig. 5.5). The tuning rods are swung in a circular arc from the cavity border to the centre by stepper motors installed at the top of the equipment (see Fig. 5.4). The stepper motors are connected to a gear reduction that converts one step into a 0.15 arcsecond rotation, which corresponds to a shift of $\sim 1\text{kHz}$ at 800MHz resonant frequency.

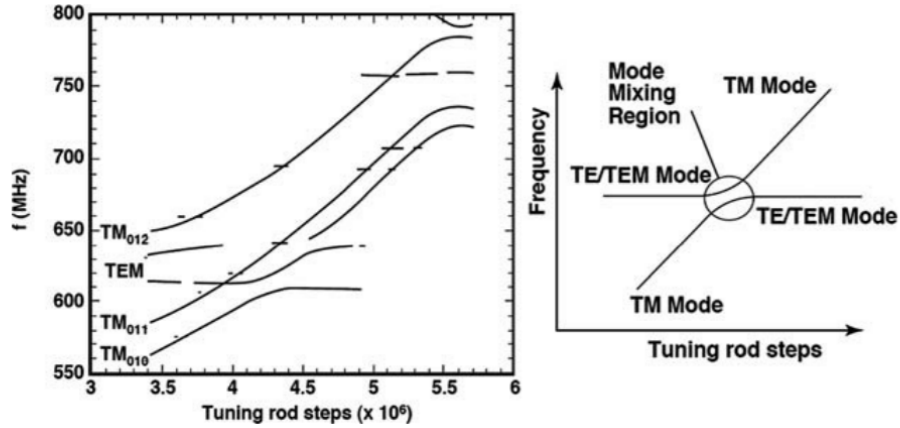


Figure 5.6 .A cavity with two copper tuning rods has a mode structure. **Left** : Resonant mode frequencies as measured with a swept RF signal when one tuning rod is held at the cavity edge and the other is moved toward the centre. **Right** : sketch of a mode crossing.

TEM modes ($B_z = E_z = 0$) can be supported in the cavity by the inclusion of metallic tuning rods. They do not couple to the axions, but they can weakly couple to the vertically mounted receiver antenna, just as the TE modes (due to imperfections in geometry, etc). The numerous resonant modes alter as a copper tuning rod is moved from near the cavity wall to the centre, as shown in Figure 5.6. The tuning-rod location has no effect on the TEM and TE modes, while the TM modes increase in frequency as one of the copper rods approaches the cavity centre. As a result, areas where a TM mode crosses a TE or TEM mode appear (referred to as mode mixing). These mode mixings (seen in the right section of Fig. 5.6) bring in new information Gaps in frequency that can't be scanned. To solve this, the cavity was eventually filled with LHe, which lowered the microwave index of refraction to 1.027, decreasing the mode crossings by 2.7% and permitting scanning of previously inaccessible frequencies. The ADMX experiment will be upgraded with a dry system in which both tuning rods are adjusted to "dance" around the mode crossover without the need of LHe.

5.3. AXION MICROCAVITY EXPERIMENT

The quality factor Q , which is a measure of the sharpness of the cavity response to external excitations, is a crucial characteristic of the resonant microwave cavity. It is a dimensionless variable that may be expressed in a variety of ways, such as the ratio of stored energy U to power loss P_L each cycle: $Q = \omega_0 U / P_L$. Sweeping a RF signal through the weakly-coupled antenna in the cavity top plate determines the quality factor Q of the TM_{010} mode (see Fig. 5.4). In most cases, the cavity’s unloaded Q is $\sim 2 \times 10^5$, which is extremely close to the theoretical maximum for oxygen-free annealed copper at cryogenic temperatures. The insertion depth of the main antenna is modified during data collection to ensure that it fits the cavity’s $50 \, \Omega$ impedance (called critically coupling). Half of the microwave power in the cavity reaches the electronics via the antenna when the antenna is critically linked, while the other half is dissipated in the cavity walls. Overcoupling the cavity lowers Q and therefore limits signal amplification, whereas undercoupling the cavity limits microwave power entering the electronics.

5.3.2.1 Gen 2/Phase IIa upgrades

The Gen 2 ADMX experiment will look for axion dark matter down to DFSZ coupling in the mass range of $2 - 40 \, \mu\text{eV}$ ($0.5 - 10 \, \text{GHz}$). Several multiyear RD projects have been formed to achieve this goal. The Cavity Working Group is working on designing and fabricating next-generation microwave cavities for higher-mass searches over the long term. To lower heat loads, piezoelectric motor drives are being tried, and tunable high-frequency SQUID amplifiers and Josephson parametric amplifiers (JPA) are being created. High-field magnets are also being studied and costed as part of the effort.

A tiered frequency mechanism will be used to reach search capabilities of more than one order of magnitude. The frequency ranges include $0.5 - 1 \, \text{GHz}$, $1 - 2 \, \text{GHz}$, $2 - 4 \, \text{GHz}$, $4 - 6 \, \text{GHz}$, $6 - 8 \, \text{GHz}$, and $8 - 10 \, \text{GHz}$. The present ADMX cavity will cover the first frequency range. The Pound stabiliser system will be used to frequency lock four cavities in the second frequency tier. The frequency locked cavities used in the 2-4 GHz and 4-6 GHz tiers will be ~ 16 and ~ 32 , respectively. A photonic band-gap cavity, a complicated system of many tuning posts that move in unison to maintain symmetry to enhance coupling, C , will be required for the $6 - 8 \, \text{GHz}$ range. The research on the ultimate tier configuration is still in its early phases. To achieve DFSZ sensitivity at greater masses, complex manufacturing techniques are used to eliminate mode mix-

5.3. AXION MICROCAVITY EXPERIMENT

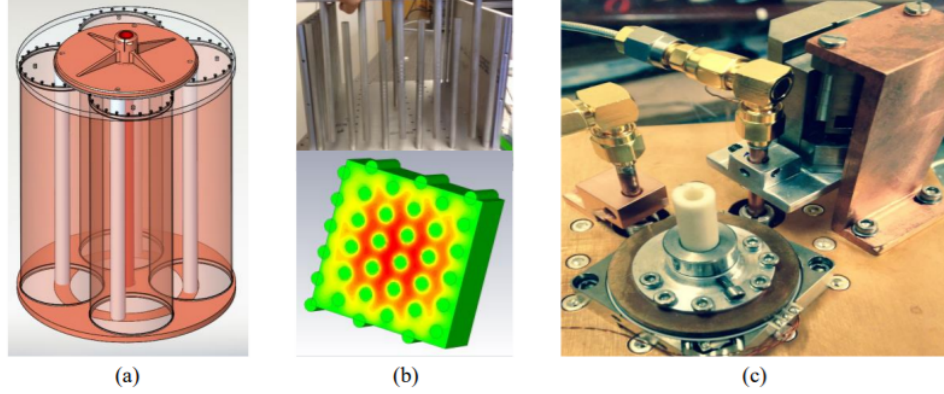


Figure 5.7 .a) A graphic representation of the cavity design for 1-2 GHz. The cavities will be frequency locked using the Pound stabiliser. b) At the top, a shot of a photonic band-gap prototype being built. Bottom: the electric field strength as a result of a simulation. The electric field will be significantly localised as symmetry is broken, resulting in a drop in C . c) Prototype of a piezoelectric motor drive.

ing and symmetry breaking, two abnormalities that drastically diminish C within the search range, while also increasing the quality factor of the cavities. Hybrid superconducting cavities are also being researched. Hybrid cavities would use superconducting thin-film coverings on the vertical surfaces to boost the detector's Q by a factor of ten. In addition, to improve scan reliability, in situ mode identification techniques and field characterization approaches are being tried. The 4-cavity concept is depicted in Figure 5.7(a – b), which includes a graphic image of a photonic band-gap cavity as well as a photograph taken inside a prototype. To address the experiment's fine motion control requirements, ADMX currently employs worm gears. The gears generate a lot of heat, which will be too much for a large number of cavities. In order to prepare for future searches, piezoelectric motor drives are being tested on the sidecar. A snapshot of the motor drive prototype is shown in Figure 5.7(c).

5.3.3 Future of Microwave Cavity Experiments

Several new search concepts for detecting dark matter axions have emerged in recent years. The NMR-based CASPER was created to investigate the mass range $10^{-6} - 10^{-9}$ eV. Other potential ideas, on the other hand, deserve a quick notice.

Rybka et al, have reported an experiment based on an open microwave resonator

5.3. AXION MICROCAVITY EXPERIMENT

structure suitable for axions in the $100 - 1,000 \mu\text{eV}$ decade, with a microwave photon wavelength ranging from 1 to 10 mm after conversion. Because the conversion probability is much increased when the applied magnetic field $B(r)$ follows the photon mode's electric field $E(r)$, a wiggler-like magnetic field with a continuously controllable periodicity is required to sweep out the mass range. Rybka et al. achieved this by employing a sequence of wire planes in an open resonator of alternating sign in current; these planes will eventually be made up of superconducting wires or stripes imprinted on a thin substrate. With couplings $> 4 \times 10^{-7} \text{ GeV}^{-1}$, the early prototype was able to rule out axions as dark matter between 68.2 and 76.5 μeV . Finally, below DFSZ axions for that mass range, sensitivity to couplings of $10^{-15} \text{ GeV}^{-1}$ should be possible.

Sikivie et al, have focused on the opposite issue of the microwave cavity experiment, namely extending the search lower in mass, where the cavity and the magnet that encloses it become unfeasibly huge below 10^{-6} eV ($\sim 250 \text{ MHz}$). The authors recommended replacing the cavity with a lumped-parameter LC circuit external to the magnetic field, stimulated by a pickup loop inside the magnet threaded by the mode's transverse magnetic field, to get around this constraint. According to the authors, this technique would be most sensitive around 10^{-7} eV , probing the band of PQ axion models, with a magnet similar to that of the existing ADMX. Such a lumped parameter LC circuit search for dark matter axions, if fully conceived and executed, might bridge a major gap where the cavity-based experiment and the NMR-based experiment may have difficulties overlapping.

The proposal for the Cosmic Axion Spin Precession Experiment (CASPER) intends to pave the way for a new route in the experimental hunt for axion dark matter. CASPER will employ nuclear magnetic resonance (NMR) methods to identify the spin precession generated by axion dark matter. This unique technique adds to prior efforts: ADMX is sensitive to higher axion frequencies, CASPER, on the other hand, will cover the lower frequencies where the axion emerges from energies $f_a \sim 10^{15} \text{ GeV} - 10^{19} \text{ GeV}$. This range is extremely difficult to approach with any other technique, while certain astrophysics techniques may be able to investigate it. A detection in such an experiment would not only mark the discovery of dark matter, but would also reveal insights into the high-energy scales from which such an axion might emerge, close to fundamental scales like the grand unification, Planck, or string scales.

CHAPTER 6

SUMMARY & CONCLUSION

This article conducts an in-depth examination of the realm of axionic dark matter. After addressing a brief history of axions, their cosmological origins, existing models, and the rationale for considering axions as cold dark matter in the first two chapters of this article, we were able to focus on studying the electromagnetic coupling of axions via the primakoff effect and calculating the three-dimensional cross-section for the scattered axion transmitted out of a Gaussian distributed magnetic field centred around the axis of a solenoid. These findings are expanded upon and used to create a comparative study of how fine tuning different parameters such as the magnetic field (B) and the radius of the solenoid (R) affects the cross section, number of events, and transmission probability of scattered axions. The results are presented in a tabular format in Table 4.1 (a), (b) ,(c).

These findings indicate that raising the energy of the incident photon from microwave to x-ray, by 5 orders of magnitude, also increases the transmission probability by approximately 19 to 17 orders of magnitude, depending on the strength of the magnetic field (B). As the energy level increases, the correlation between Radius and the axion transmission probability P_{trans} weakens. i.e A tenfold increase in the radius R of the solenoids raises the P_{trans} by five orders of magnitude for visible and microwave photons, but only by three orders of magnitude for X rays.

By examining the behaviour of equation 4.17, which is the transmitted axion cross-section σ_{tot} , using Python data analysis and graphing libraries such as matplotlib, numpy, and scipy, we conclude that a tenfold increase in the K, R, and B values results in a sevenfold increase in the cross-section. This is due primarily to the modified Bessel function and the exponential term with K and R arguments. Further decomposing equation 4.17 by holding all other variables constant and adjusting only the K and R variables one at a time and plotting it against the cross section σ_{tot} reveals that the slope difference between both of these plots presented in figure 4.3 allows us to fine-tune the experiment for the desired axion conversion probability.

Chapter 5 presents a full review of the axion studies based on the inverse primakoff principle. We address the quest to discover the solar axion through a variety of studies and collaborations. Using axion telescopes such as CAST and SUMICO, as well as X-ray telescopes, which investigate the limitations of the axion photon coupling constant and mass. CAST recently released a work in which they established an upper limit of $g_{\phi\gamma\gamma} < 0.66 \times 10^{-10} \text{ GeV}^{-1}$ for m_ϕ smaller than 0.02 eV with a 95 % confidence level. This is the highest level of performance yet achieved by a laboratory limit helioscope.

Additionally, this thesis discussed cutting-edge research being conducted on Axion Microcavity Experiments such as BNL, CARRACK, and ADMX, as well as their upcoming enhancements. Microcavity experiments may now explore a range of 10^6 to 10^9 eV using current technology. ADMX and CASPER will work in tandem to cover higher and lower accident frequencies that are difficult to approach with other techniques. This will increase the likelihood of Axion discovery in the near future and may also aid in probing more fundamental energy scales.

It's important to remember that finding the axion would not only answer the Strong-CP problem and shed light on the nature of dark matter, but it might also open up new vistas in astrophysics, cosmology, and quantum physics. There may be fresh insights into the creation of the Milky Way if fine structure is discovered in the axion spectrum. In fact, because of the axion's large de Broglie wavelength ($\lambda_a \sim 10\text{--}100 \text{ m}$), fascinating quantum experiments might be carried out at macroscopic scales. The axion is a very intriguing dark matter candidate because of all of these intriguing possibilities that are within reach of present and near-future technology.

Bibliography

- [1] T. P. Cheng and L. F. Li, “GAUGE THEORY OF ELEMENTARY PARTICLE PHYSICS,” ISBN:”978-0-19-851961-4”,1984
- [2] J. F. Donoghue, E. Golowich and B. R. Holstein, “Dynamics of the standard model,” Camb. Monogr. Part. Phys. Nucl. Phys. Cosmol. **2**, 1-540 (1992) doi:10.1017/CBO9780511524370
- [3] G. ’t Hooft, “Computation of the Quantum Effects Due to a Four-Dimensional Pseudoparticle,” Phys. Rev. D **14** (1976), 3432-3450 [erratum: Phys. Rev. D **18** (1978), 2199] doi:10.1103/PhysRevD.14.3432
- [4] J. M. Pendlebury, S. Afach, N. J. Ayres, C. A. Baker, G. Ban, G. Bison, K. Bodek, M. Burghoff, P. Geltenbort and K. Green, *et al.* ”Revised experimental upper limit on the electric dipole moment of the neutron,” Phys. Rev. D **92**, no.9, 092003 (2015) doi:10.1103/PhysRevD.92.092003 [arXiv:1509.04411 [hep-ex]].
- [5] V. Baluni, “CP Violating Effects in QCD,” Phys. Rev. D **19**, 2227-2230 (1979) doi:10.1103/PhysRevD.19.2227
- [6] R. J. Crewther, P. Di Vecchia, G. Veneziano and E. Witten, “Chiral Estimate of the Electric Dipole Moment of the Neutron in Quantum Chromodynamics,” Phys. Lett. B **88**, 123 (1979) [erratum: Phys. Lett. B **91**, 487 (1980)] doi:10.1016/0370-2693(79)90128-X
- [7] R. D. Peccei and H. R. Quinn, “CP Conservation in the Presence of Instantons,” Phys. Rev. Lett. **38**, 1440-1443 (1977) doi:10.1103/PhysRevLett.38.1440
- [8] R. D. Peccei and H. R. Quinn, “Constraints Imposed by CP Conservation in the Presence of Instantons,” Phys. Rev. D **16**, 1791-1797 (1977) doi:10.1103/PhysRevD.16.1791
- [9] S. Weinberg, “A New Light Boson?,” Phys. Rev. Lett. **40**, 223-226 (1978) doi:10.1103/PhysRevLett.40.223
- [10] F. Wilczek, “Problem of Strong P and T Invariance in the Presence of Instantons,” Phys. Rev. Lett. **40**, 279-282 (1978) doi:10.1103/PhysRevLett.40.279

BIBLIOGRAPHY

- [11] C. Vafa and E. Witten, “Parity Conservation in QCD,” *Phys. Rev. Lett.* **53**, 535 (1984) doi:10.1103/PhysRevLett.53.535
- [12] J. E. Kim, “Light Pseudoscalars, Particle Physics and Cosmology,” *Phys. Rept.* **150**, 1-177 (1987) doi:10.1016/0370-1573(87)90017-2
- [13] G. G. Raffelt, “Axions in astrophysics and cosmology,” [arXiv:hep-ph/9502358 [hep-ph]].
- [14] M. S. Turner, “Windows on the Axion,” *Phys. Rept.* **197**, 67-97 (1990) doi:10.1016/0370-1573(90)90172-X
- [15] M. Dine, W. Fischler and M. Srednicki, “A Simple Solution to the Strong CP Problem with a Harmless Axion,” *Phys. Lett. B* **104**, 199-202 (1981) doi:10.1016/0370-2693(81)90590-6
- [16] J. E. Kim, “Weak Interaction Singlet and Strong CP Invariance,” *Phys. Rev. Lett.* **43**, 103 (1979) doi:10.1103/PhysRevLett.43.103
- [17] M. A. Shifman, A. I. Vainshtein and V. I. Zakharov, “Can Confinement Ensure Natural CP Invariance of Strong Interactions?,” *Nucl. Phys. B* **166**, 493-506 (1980) doi:10.1016/0550-3213(80)90209-6
- [18] A. R. Zhitnitsky, “On Possible Suppression of the Axion Hadron Interactions. (In Russian),” *Sov. J. Nucl. Phys.* **31**, 260 (1980)
- [19] L. F. Abbott and P. Sikivie, “A Cosmological Bound on the Invisible Axion,” *Phys. Lett. B* **120**, 133-136 (1983) doi:10.1016/0370-2693(83)90638-X
- [20] M. Dine and W. Fischler, “The Not So Harmless Axion,” *Phys. Lett. B* **120**, 137-141 (1983) doi:10.1016/0370-2693(83)90639-1
- [21] J. Preskill, M. B. Wise and F. Wilczek, “Cosmology of the Invisible Axion,” *Phys. Lett. B* **120**, 127-132 (1983) doi:10.1016/0370-2693(83)90637-8
- [22] D. N. Schramm and M. S. Turner, “Big Bang Nucleosynthesis Enters the Precision Era,” *Rev. Mod. Phys.* **70**, 303-318 (1998) doi:10.1103/RevModPhys.70.303 [arXiv:astro-ph/9706069 [astro-ph]].
- [23] Tegmark, M., et al. [SDSS Collaboration]: Cosmological parameters from SDSS and WMAP. *Phys. Rev. D* **69**, 103501 (2004) [astro-ph/0310723] 135

BIBLIOGRAPHY

- [24] F. Zwicky, “On the Masses of Nebulae and of Clusters of Nebulae,” *Astrophys. J.* **86**, 217-246 (1937) doi:10.1086/143864
- [25] K. Griest and M. Kamionkowski, “Supersymmetric dark matter,” *Phys. Rept.* **333**, 167-182 (2000) doi:10.1016/S0370-1573(00)00021-1
- [26] Spergel, D.N., et al. [WMAP Collaboration]: First year Wilkinson microwave anisotropy probe (WMAP) observations: Determination of cosmological parameters. *Astrophys. J. Suppl.* **148**, 175 (2003) [astro-ph/0302209] 135
- [27] Primack, J.R.: Dark matter and structure formation in the universe. In: *Proceedings of Midrasha Matematicae in Jerusalem: Winter School in Dynamic Systems* (1997), [astro-ph/9707285] 136
- [28] E. I. Gates, G. Gyuk and M. S. Turner, “The Local halo density,” *Astrophys. J. Lett.* **449**, L123-L126 (1995) doi:10.1086/309652 [arXiv:astro-ph/9505039 [astro-ph]].
- [29] M. Burghoff, A. Schnabel, G. Ban, T. Lefort, Y. Lemiere, O. Naviliat-Cuncic, E. Pierre, G. Quemener, J. Zejma and M. Kasprzak, *et al.* “An Improved Search for the Neutron Electric Dipole Moment,” [arXiv:1110.1505 [nucl-ex]].
- [30] R. Bradley, J. Clarke, D. Kinion, L. J. Rosenberg, K. van Bibber, S. Matsuki, M. Muck and P. Sikivie, “Microwave cavity searches for dark-matter axions,” *Rev. Mod. Phys.* **75**, 777-817 (2003) doi:10.1103/RevModPhys.75.777
- [31] Sikivie, P.: Evidence for ring caustics in the Milky Way. *Phys. Lett. B* **567**, 1 (2003) [astro-ph/0109296] 137
- [32] P. Svrcek and E. Witten, “Axions In String Theory,” *JHEP* **06**, 051 (2006) doi:10.1088/1126-6708/2006/06/051 [arXiv:hep-th/0605206 [hep-th]].
- [33] A. D. Linde, “Axions in inflationary cosmology,” *Phys. Lett. B* **259**, 38-47 (1991) doi:10.1016/0370-2693(91)90130-I
- [34] F. Wilczek, “A Model of anthropic reasoning, addressing the dark to ordinary matter coincidence,” [arXiv:hep-ph/0408167 [hep-ph]].
- [35] M. Tegmark, A. Aguirre, M. Rees and F. Wilczek, “Dimensionless constants, cosmology and other dark matters,” *Phys. Rev. D* **73**, 023505 (2006) doi:10.1103/PhysRevD.73.023505 [arXiv:astro-ph/0511774 [astro-ph]].

BIBLIOGRAPHY

- [36] M. P. Hertzberg, M. Tegmark and F. Wilczek, “Axion Cosmology and the Energy Scale of Inflation,” *Phys. Rev. D* **78**, 083507 (2008) doi:10.1103/PhysRevD.78.083507 [arXiv:0807.1726 [astro-ph]].
- [37] J. Hamann, S. Hannestad, G. G. Raffelt and Y. Y. Y. Wong, “Isocurvature forecast in the anthropic axion window,” *JCAP* **06**, 022 (2009) doi:10.1088/1475-7516/2009/06/022 [arXiv:0904.0647 [hep-ph]].
- [38] L. J. Rosenberg and K. A. van Bibber, “Searches for invisible axions,” *Phys. Rept.* **325**, 1-39 (2000) doi:10.1016/S0370-1573(99)00045-9
- [39] R. L. Davis, “Goldstone Bosons in String Models of Galaxy Formation,” *Phys. Rev. D* **32**, 3172 (1985) doi:10.1103/PhysRevD.32.3172
- [40] R. L. Davis, “Cosmic Axions from Cosmic Strings,” *Phys. Lett. B* **180**, 225-230 (1986) doi:10.1016/0370-2693(86)90300-X
- [41] D. Harari and P. Sikivie, “On the Evolution of Global Strings in the Early Universe,” *Phys. Lett. B* **195**, 361-365 (1987) doi:10.1016/0370-2693(87)90032-3
- [42] A. Vilenkin and T. Vachaspati, “Radiation of Goldstone Bosons From Cosmic Strings,” *Phys. Rev. D* **35**, 1138 (1987) doi:10.1103/PhysRevD.35.1138
- [43] R. L. Davis and E. P. S. Shellard, “DO AXIONS NEED INFLATION?,” *Nucl. Phys. B* **324**, 167-186 (1989) doi:10.1016/0550-3213(89)90187-9
- [44] A. Dabholkar and J. M. Quashnock, “Pinning Down the Axion,” *Nucl. Phys. B* **333**, 815-832 (1990) doi:10.1016/0550-3213(90)90140-9
- [45] R. A. Battye and E. P. S. Shellard, “Global string radiation,” *Nucl. Phys. B* **423**, 260-304 (1994) doi:10.1016/0550-3213(94)90573-8 [arXiv:astro-ph/9311017 [astro-ph]].
- [46] R. A. Battye and E. P. S. Shellard, “Axion string constraints,” *Phys. Rev. Lett.* **73**, 2954-2957 (1994) [erratum: *Phys. Rev. Lett.* **76**, 2203-2204 (1996)] doi:10.1103/PhysRevLett.73.2954 [arXiv:astro-ph/9403018 [astro-ph]].
- [47] M. Yamaguchi, M. Kawasaki and J. Yokoyama, “Evolution of axionic strings and spectrum of axions radiated from them,” *Phys. Rev. Lett.* **82**, 4578-4581 (1999) doi:10.1103/PhysRevLett.82.4578 [arXiv:hep-ph/9811311 [hep-ph]].

BIBLIOGRAPHY

- [48] C. Hagmann, S. Chang and P. Sikivie, “Axion radiation from strings,” *Phys. Rev. D* **63**, 125018 (2001) doi:10.1103/PhysRevD.63.125018 [arXiv:hep-ph/0012361 [hep-ph]].
- [49] S. Chang, C. Hagmann and P. Sikivie, “Studies of the motion and decay of axion walls bounded by strings,” *Phys. Rev. D* **59**, 023505 (1999) doi:10.1103/PhysRevD.59.023505 [arXiv:hep-ph/9807374 [hep-ph]].
- [50] D. H. Lyth, “Estimates of the cosmological axion density,” *Phys. Lett. B* **275**, 279-283 (1992) doi:10.1016/0370-2693(92)91590-6
- [51] M. Nagasawa and M. Kawasaki, “Collapse of axionic domain wall and axion emission,” *Phys. Rev. D* **50**, 4821-4826 (1994) doi:10.1103/PhysRevD.50.4821 [arXiv:astro-ph/9402066 [astro-ph]].
- [52] P. Sikivie, “Axion Cosmology,” *Lect. Notes Phys.* **741**, 19-50 (2008) doi:10.1007/978-3-540-73518-2_2 [arXiv:astro-ph/0610440 [astro-ph]].
- [53] D. J. Gross, R. D. Pisarski and L. G. Yaffe, “QCD and Instantons at Finite Temperature,” *Rev. Mod. Phys.* **53**, 43 (1981) doi:10.1103/RevModPhys.53.43
- [54] C. Hagmann and P. Sikivie, “Computer simulations of the motion and decay of global strings,” *Nucl. Phys. B* **363**, 247-280 (1991) doi:10.1016/0550-3213(91)90243-Q
- [55] P. Sikivie, “Of Axions, Domain Walls and the Early Universe,” *Phys. Rev. Lett.* **48**, 1156-1159 (1982) doi:10.1103/PhysRevLett.48.1156
- [56] H. Georgi and M. B. Wise, “Hiding the Invisible Axion,” *Phys. Lett. B* **116**, 123-126 (1982) doi:10.1016/0370-2693(82)90989-3 [57]
- [57] P. Sikivie, *Phys. Rev. Lett.* **51**, 1415-1417 (1983) [erratum: *Phys. Rev. Lett.* **52**, 695 (1984)] doi:10.1103/PhysRevLett.51.1415
- [58] P. Sikivie, “Detection Rates for ‘Invisible’ Axion Searches,” *Phys. Rev. D* **32**, 2988 (1985) [erratum: *Phys. Rev. D* **36**, 974 (1987)] doi:10.1103/PhysRevD.36.974
- [59] H. Primakoff, “Photoproduction of neutral mesons in nuclear electric fields and the mean life of the neutral meson,” *Phys. Rev.* **81**, 899 (1951) doi:10.1103/PhysRev.81.899

BIBLIOGRAPHY

- [60] Y. Inoue, Y. Akimoto, R. Ohta, T. Mizumoto, A. Yamamoto and M. Minowa, “Search for solar axions with mass around 1 eV using coherent conversion of axions into photons,” *Phys. Lett. B* **668**, 93-97 (2008) doi:10.1016/j.physletb.2008.08.020 [arXiv:0806.2230 [astro-ph]].
- [61] E. Arik *et al.* [CAST], “Probing eV-scale axions with CAST,” *JCAP* **02**, 008 (2009) doi:10.1088/1475-7516/2009/02/008 [arXiv:0810.4482 [hep-ex]].
- [62] R. Ballou *et al.* [OSQAR], *Phys. Rev. D* **92**, no.9, 092002 (2015) doi:10.1103/PhysRevD.92.092002 [arXiv:1506.08082 [hep-ex]].
- [63] G. G. Raffelt, “Stars as laboratories for fundamental physics: The astrophysics of neutrinos, axions, and other weakly interacting particles,” ISBN: 9780226702728
- [64] S. De Panfilis, A. C. Melissinos, B. E. Moskowitz, J. T. Rogers, Y. K. Semertzidis, W. Wuensch, H. J. Halama, A. G. Prodel, W. B. Fowler and F. A. Nezrick, “Limits on the Abundance and Coupling of Cosmic Axions at 4.5-Microev $< m(a) < 5.0$ -Microev,” *Phys. Rev. Lett.* **59**, 839 (1987) doi:10.1103/PhysRevLett.59.839
- [65] W. Wuensch, S. De Panfilis-Wuensch, Y. K. Semertzidis, J. T. Rogers, A. C. Melissinos, H. J. Halama, B. E. Moskowitz, A. G. Prodel, W. B. Fowler and F. A. Nezrick, “Results of a Laboratory Search for Cosmic Axions and Other Weakly Coupled Light Particles,” *Phys. Rev. D* **40**, 3153 (1989) doi:10.1103/PhysRevD.40.3153
- [66] C. Hagmann, P. Sikivie, N. S. Sullivan and D. B. Tanner, “Results from a search for cosmic axions,” *Phys. Rev. D* **42**, 1297-1300 (1990) doi:10.1103/PhysRevD.42.1297
- [67] S. J. Asztalos *et al.* [ADMX], “An Improved RF cavity search for halo axions,” *Phys. Rev. D* **69**, 011101 (2004) doi:10.1103/PhysRevD.69.011101 [arXiv:astro-ph/0310042 [astro-ph]].
- [68] M. Tada, Y. Kishimoto, K. Kominato, M. Shibata, H. Funahashi, K. Yamamoto, A. Masaike and S. Matsuki, “CARRACK II: A new large scale experiment to search for axions with Rydberg-atom cavity detector,” *Nucl. Phys. B Proc. Suppl.* **72**, 164-168 (1999) doi:10.1016/S0920-5632(98)00519-2

BIBLIOGRAPHY

- [69] G. G. Raffelt, “Astrophysical axion bounds,” *Lect. Notes Phys.* **741**, 51-71 (2008) doi:10.1007/978-3-540-73518-2_3 [arXiv:hep-ph/0611350 [hep-ph]].
- [70] Miller Bertolami, Marcelo Melendez, Brenda Althaus, Leandro Isern, Jordi. (2014). Revisiting the axion bounds from the Galactic white dwarf luminosity function. *Journal of Cosmology and Astroparticle Physics*. 2014. 10.1088/1475-7516/2014/10/069.
- [71] Isern, J. Garcia-Berro, Enrique Althaus, Leandro Córscico, Alejandro. (2010). Axions and the pulsation periods of variable white dwarfs revisited (Research Note). *Astron. Astrophys.* 512. 10.1051/0004-6361/200913716.
- [72] Córscico, Alejandro Althaus, Leandro Romero, Alejandra Mukadam, A.S. Garcia-Berro, Enrique Isern, J. Kepler, S. Corti, M.A.. (2012). An independent limit on the axion mass from the variable white dwarf star R548. *Journal of Cosmology and Astroparticle Physics*. 2012. 010.
- [73] Igor G. Irastorza, Javier Redondo, Graham, P., Irastorza, I., Lamoreaux, S., Lindner, A., Bibber, K. (2015). Experimental Searches for the Axion and Axion-Like Particles. *Annual Review of Nuclear and Particle Science*, 65, 485-514.
- [74] Lazarus, D.M., Smith, G.C., Cameron, R., Melissinos, A.C., Ruoso, G., Semertzidis, Y.K., Nezzrick, F.A.: A search for solar axions. *Phys. Rev. Lett.* **69**, 2333(1992) 204,205,206,233
- [75] Y. Inoue, T. Namba, S. Moriyama, M. Minowa, Y. Takasu, T. Horiuchi and A. Yamamoto, “Search for sub-electronvolt solar axions using coherent conversion of axions into photons in magnetic field and gas helium,” *Phys. Lett. B* **536**, 18-23 (2002) doi:10.1016/S0370-2693(02)01822-1 [arXiv:astro-ph/0204388 [astro-ph]].
- [76] P. Abbon, S. Andriamonje, S. Aune, T. Dafni, M. Davenport, E. Delagnes, R. d. Oliveira, G. Fanourakis, E. F. Ribas and J. Franz, *et al.* “The Micromegas detector of the CAST experiment,” *New J. Phys.* **9**, 170 (2007) doi:10.1088/1367-2630/9/6/170 [arXiv:physics/0702190 [physics]].
- [77] M. Kuster, H. Bräuninger, S. Cebrián, M. Davenport, C. Eleftheriadis, J. Englhauser, H. Fischer, J. Franz, P. Friedrich and R. Hartmann, *et al.* “The X-ray Telescope of CAST,” *New J. Phys.* **9**, 169 (2007) doi:10.1088/1367-2630/9/6/169 [arXiv:physics/0702188 [physics.ins-det]].

BIBLIOGRAPHY

- [78] D. Autiero, B. Beltrán, J. M. Carmona, S. Cebrián, E. Chesi, M. Davenport, M. Delattre, L. D. Lella, F. Formenti and I. G. Irastorza, *et al.* “The CAST Time Projection Chamber,” *New J. Phys.* **9**, 171 (2007) doi:10.1088/1367-2630/9/6/171 [arXiv:physics/0702189 [physics.ins-det]].
- [79] H. Davoudiasl and P. Huber, “Detecting solar axions using earth’s magnetic field,” *Phys. Rev. Lett.* **97**, 141302 (2006) doi:10.1103/PhysRevLett.97.141302 [arXiv:hep-ph/0509293 [hep-ph]].
- [80] I. G. Hannah, G. J. Hurford, H. S. Hudson, R. P. Lin and K. van Bibber, “First limits on the 3-200 keV X-ray spectrum of the quiet Sun using RHESSI,” *Astrophys. J. Lett.* **659**, L77-L80 (2007) doi:10.1086/516750 [arXiv:astro-ph/0702726 [astro-ph]].
- [81] I. G. Hannah, S. Christe, S. Krucker, G. J. Hurford, H. S. Hudson and R. P. Lin, “RHESSI Microflare Statistics. 2. X-ray Imaging, Spectroscopy & Energy Distributions,” *Astrophys. J.* **677**, 704 (2008) doi:10.1086/529012 [arXiv:0712.2544 [astro-ph]].
- [82] Antolin, P., Shibata, K., Kudoh, T., Shiota, D., Brooks, D. 2010. Signatures of Coronal Heating Mechanisms. *Astrophysics and Space Science Proceedings* 19, 277–280. doi:10.1007/978-3-642-02859-5_21
- [83] E. D. Carlson and L. S. Tseng, “Pseudoscalar conversion and x-rays from the sun,” *Phys. Lett. B* **365**, 193-201 (1996) doi:10.1016/0370-2693(95)01250-8 [arXiv:hep-ph/9507345 [hep-ph]].
- [84] Kuster, Markus. (2008). *Axions - Theory, Cosmology and Experimental Searches*. 10.1007/978-3-540-73518-2.
- [85] R. H. Dicke, *Rev. Sci. Instrum.* **17**, no.7, 268-275 (1946) doi:10.1063/1.1770483
- [86] L. D. Duffy and K. van Bibber, “Axions as Dark Matter Particles,” *New J. Phys.* **11**, 105008 (2009) doi:10.1088/1367-2630/11/10/105008 [arXiv:0904.3346 [hep-ph]].
- [87] S. De Panfilis, A. C. Melissinos, B. E. Moskowitz, J. T. Rogers, Y. K. Semertzidis, W. Wuensch, H. J. Halama, A. G. Prodell, W. B. Fowler and F. A. Nezrick, “Limits on the Abundance and Coupling of Cosmic Axions at $4.5\text{-Microev} < m(a) < 5.0\text{-Microev}$,” *Phys. Rev. Lett.* **59**, 839 (1987) doi:10.1103/PhysRevLett.59.839

BIBLIOGRAPHY

- [88] Tada, M. Kishimoto, Y. Kominato, Kentaro Shibata, M. Yamada, Shunich Haseyama, Tomohito Ogawa, I. Funahashi, H. Yamamoto, Kazami Matsuki, S.. (2006). Single-photon detection of microwave blackbody radiations in a low-temperature resonant-cavity with high Rydberg atoms. *Physics Letters A*. 349. 488-493. 10.1016/j.physleta.2005.09.066.
- [89] D. S. Kinion, “First results from a multiple microwave cavity search for dark matter axions,” UMI-30-19020.
- [90] R. V. Pound, ”Frequency Stabilization of Microwave Oscillators,” in *Proceedings of the IRE*, vol. 35, no. 12, pp. 1405-1415, Dec. 1947, doi: 10.1109/JR-PROC.1947.226198.
- [91] Rybka, Gray Wagner, Andrew Patel, Kunal Percival, Robert Ramos, Katleiah Brill, Aryeh. (2015). Search for dark matter axions with the Orpheus experiment. *Physical Review D*. 91. 10.1103/PhysRevD.91.011701.
- [92] Sikivie, P Sullivan, Neil Tanner, David. (2014). Proposal for Axion Dark Matter Detection Using an LC Circuit. *Physical review letters*. 112. 131301. 10.1103/PhysRevLett.112.131301.
- [93] Baker, Oliver Betz, Michael Caspers, Fritz Jaeckel, Joerg Lindner, Axel Ringwald, Andreas Semertzidis, Yannis Sikivie, Pierre Zioutas, Konstantin. (2012). Prospects for searching axionlike particle dark matter with dipole, toroidal, and wiggler magnets. *Phys. Rev. D*. 85. 10.1103/PhysRevD.85.035018.
- [94] Horns, Dieter Jaeckel, Joerg Lindner, Axel Lobanov, Andrei Redondo, Javier Ringwald, Andreas. (2012). Searching for WISPy Cold Dark Matter with a Dish Antenna. *Journal of Cosmology and Astro-Particle Physics*. 2013. 10.1088/1475-7516/2013/04/016.

APPENDIX A

Python Plots and Codes

A.1 3D plots

A.1.1 σ_{tot} vs B vs R plot

PYTHON CODE :

```
#importing the essential libraries
from mpl_toolkits import mplot3d
import scipy.special as spl
import numpy as np
import matplotlib.pyplot as plt
import matplotlib.ticker as mtick

#assigning the constant values for the cross section plot;
w=124
L=10
g=8.8E-20
y=124

#defining our cross section function as z(x,y);
def z_function(x, B):
    return (np.sqrt(2*np.pi))*((y*L*g*B*(pow(x,2)))**2 * (1/16))*y*pow(
        x, 5)*np.exp(-(y**2)*(x**2))*
        spl.iv(0.5,(y**2)*(x**2)))

#defining our variables- R=x and B=y;
x = np.linspace(0, 0.2, 100)
B = np.linspace(0, 1950, 100)

#mapping the function z(x,y) to meshgrid Z(X,Y)
X, Y = np.meshgrid(x, B)
Z = z_function(X, Y)
```

A.1. 3D plots

```
#plotting wireframe plot Z(X,Y)
fig = plt.figure(figsize=(20,20))
ax = plt.axes(projection="3d")
ax.plot_wireframe(X, Y, Z, cmap='autumn')
ax.view_init(32.5,-75)
#labeling the axis for wireframe
ax.set_xlabel('solenoid Radius (R)' + r'$\rightarrow$')
ax.set_ylabel('Magnetic field (B)' + r'$\rightarrow$')
ax.set_zlabel('Cross section ( $\mu_0 I_{tot}$ )' + r'$\rightarrow$')
plt.gca().zaxis.set_major_formatter(mtick.FormatStrFormatter('%0.0e'))

#fixing the figure size and zaxis format
fig = plt.figure(figsize=(20,20))
ax = plt.axes(projection='3d')
plt.gca().zaxis.set_major_formatter(mtick.FormatStrFormatter('%0.0e'))

#plotting Z(X,Y) with color bar
surf=ax.plot_surface(X, Y, Z, rstride=1, cstride=1,
                    cmap='rainbow', edgecolor='none')
fig.colorbar(surf,shrink=0.5,aspect=7)
ax.view_init(32.5,-75)
#labeling the axis for surface plot
ax.set_xlabel('solenoid Radius (R)' + r'$\rightarrow$')
ax.set_ylabel('Magnetic field (B)' + r'$\rightarrow$')
ax.set_zlabel('Cross section ( $\mu_0 I_{tot}$ )' + r'$\rightarrow$')

#fixing the figure size and zaxis format
fig = plt.figure(figsize=(20,20))
ax = plt.axes(projection="3d")
plt.gca().zaxis.set_major_formatter(mtick.FormatStrFormatter('%0.0e'))

#plotting Z(X,Y) with color bar
qcs=plt.contourf(X, Y, Z,20, cmap='rainbow')
plt.colorbar(qcs,shrink=0.5,aspect=7)
ax.view_init(32.5,-75)
#labeling the axis for countour plot
ax.set_xlabel('solenoid Radius (R)' + r'$\rightarrow$')
ax.set_ylabel('Magnetic field (B)' + r'$\rightarrow$')
ax.set_zlabel('Cross section ( $\mu_0 I_{tot}$ )' + r'$\rightarrow$')
#display our 3d plots
plt.show()
```

A.1. 3D plots

OUTPUT :

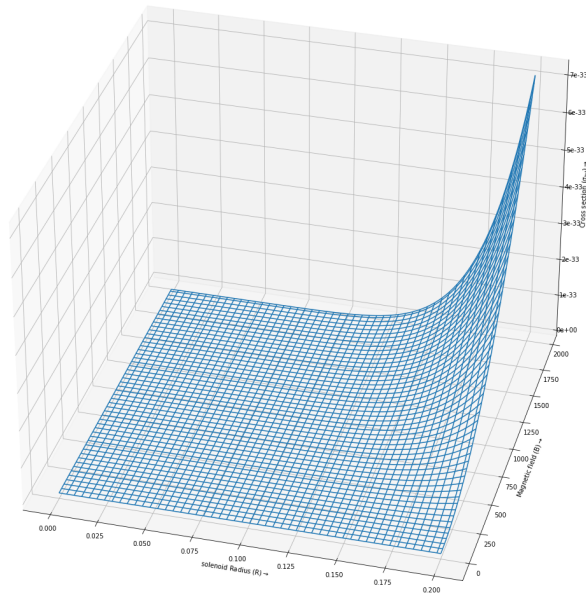


Figure 7.1(a) : wireframe.

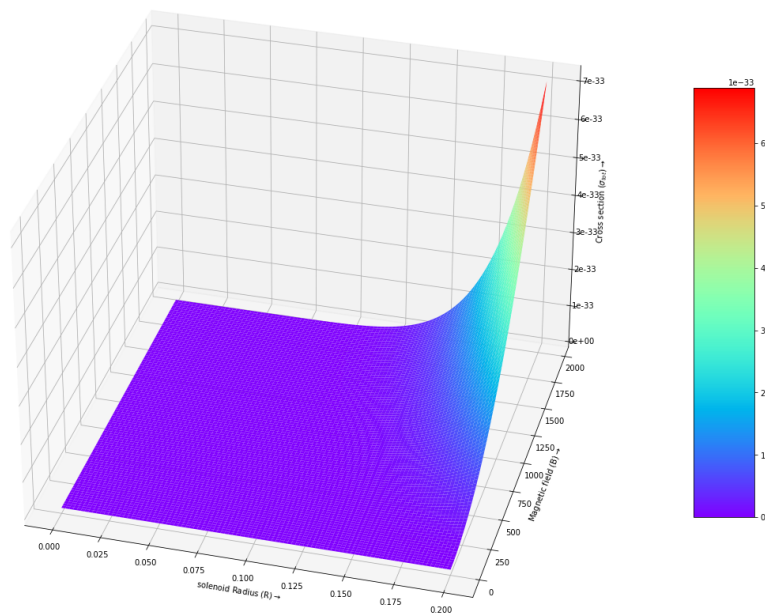


Figure 7.1(b) : surface.

A.1. 3D plots

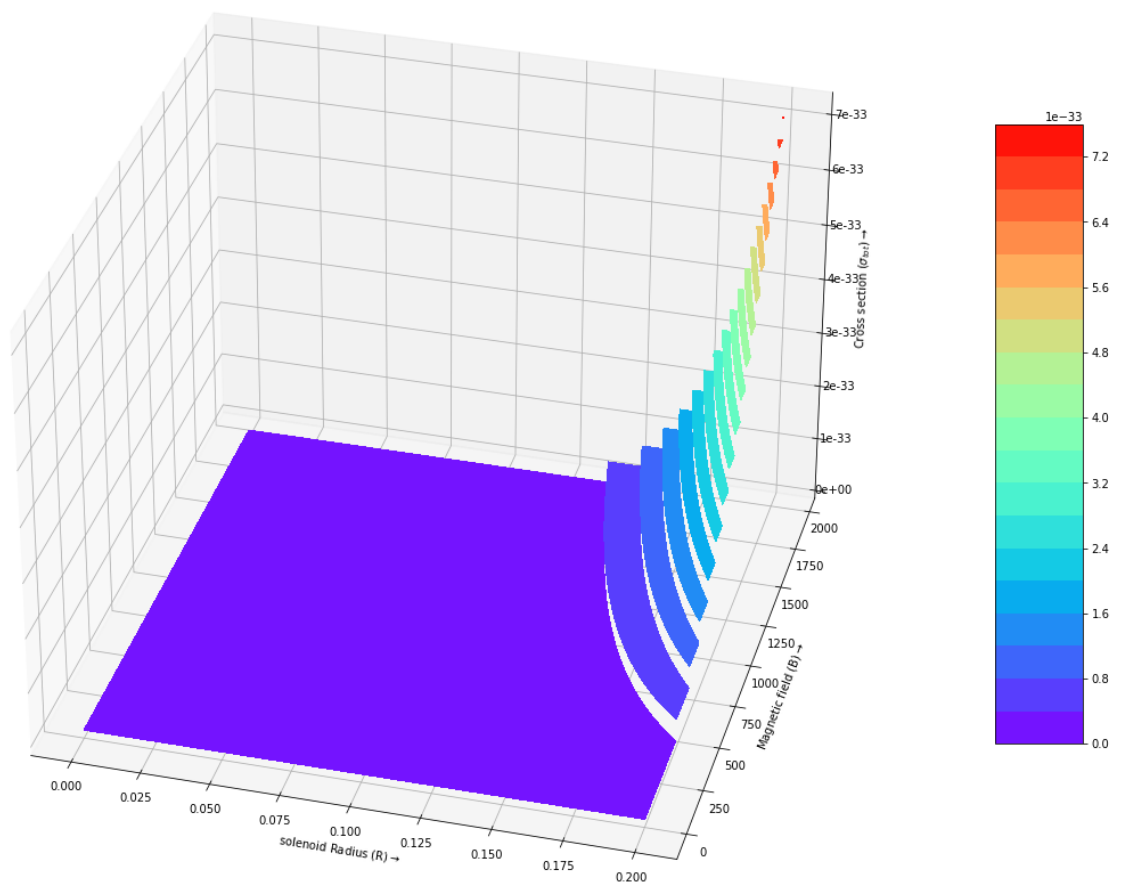


Figure 7.1(c) : contour.

A.1. 3D plots

A.1.2 σ_{tot} vs K vs R plot

PYTHON CODE :

```
#importing the essential libraries
from mpl_toolkits import mplot3d
import scipy.special as spl
import numpy as np
import matplotlib.pyplot as plt
import matplotlib.ticker as mtick

#assigning the constant values for the cross section plot;
B = 1950
w=124
L=10
g=8.8E-20

#defining our cross section function as z(x,y);
def z_function(x, y):
    return (np.sqrt(2*np.pi)*((y*L*g*B*(pow(x,2)))**2*(1/16))*y*pow(x,
        5)*np.exp(-(y**2)*(x**2))*spl.
        iv(0.5,(y**2)*(x**2)))

#defining our variables- R=x and K=y;
x = np.linspace(0, 0.2, 100)
y = np.linspace(0, 125, 100)

#mapping the function z(x,y) to meshgrid Z(X,Y)
X, Y = np.meshgrid(x, y)
Z = z_function(X, Y)

#plotting wireframe plot Z(X,Y)
fig = plt.figure(figsize=(20,20))
ax = plt.axes(projection="3d")
ax.plot_wireframe(X, Y, Z, cmap='autumn')
#labeling the axis for wireframe
ax.set_xlabel('solenoid Radius (R)'+ r'$\rightarrow$')
ax.set_ylabel('Photon momentum (K)'+ r'$\rightarrow$')
ax.set_zlabel('Cross section ( $\sigma_{tot}$ )'+ r'$\rightarrow$')
plt.gca().zaxis.set_major_formatter(mtick.FormatStrFormatter('%0e'))

#fixing the figure size and zaxis format
```


A.1. 3D plots

```
fig = plt.figure(figsize=(20,20))
ax = plt.axes(projection='3d')
plt.gca().zaxis.set_major_formatter(mtick.FormatStrFormatter('%.0e'))
ax.view_init(32.5,-75)
#plotting Z(X,Y) with color bar
surf=ax.plot_surface(X, Y, Z, rstride=1, cstride=1,
                    cmap='rainbow', edgecolor='none')
fig.colorbar(surf,shrink=0.5,aspect=7)
ax.view_init(32.5,-75)
#labeling the axis for surface plot
ax.set_xlabel('solenoid Radius (R)' + r'$\rightarrow$')
ax.set_ylabel('Photon momentum (K)' + r'$\rightarrow$')
ax.set_zlabel('Cross section ( $\sigma_{tot}$ )' + r'$\rightarrow$')

#fixing the figure size and zaxis format
fig = plt.figure(figsize=(20,20))
ax = plt.axes(projection="3d")
plt.gca().zaxis.set_major_formatter(mtick.FormatStrFormatter('%.0e'))

#plotting Z(X,Y) with color bar
qcs=plt.contourf(X, Y, Z,20, cmap='rainbow')
plt.colorbar(qcs,shrink=0.5,aspect=7)
ax.view_init(32.5,-75)
#labeling the axis for countour plot
ax.set_xlabel('solenoid Radius (R)' + r'$\rightarrow$')
ax.set_ylabel('Photon momentum (K)' + r'$\rightarrow$')
ax.set_zlabel('Cross section ( $\sigma_{tot}$ )' + r'$\rightarrow$')

#display the 3d plots
plt.show()
```

A.1. 3D plots

OUTPUT :

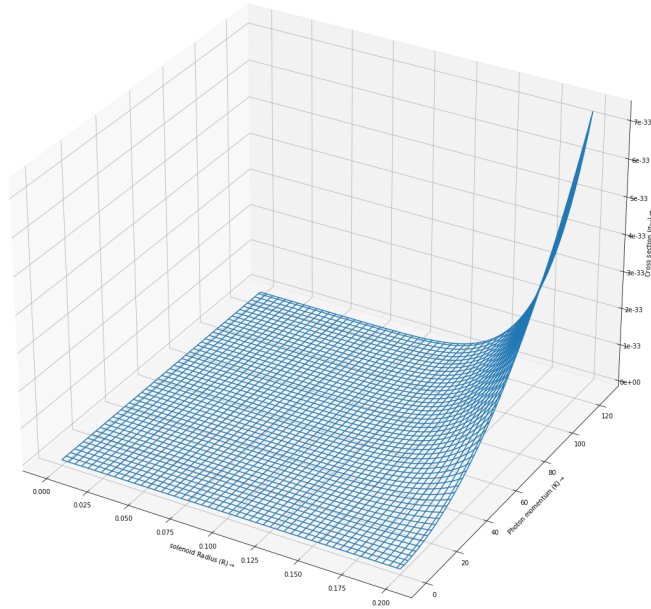


Figure 7.2(a) : wireframe.

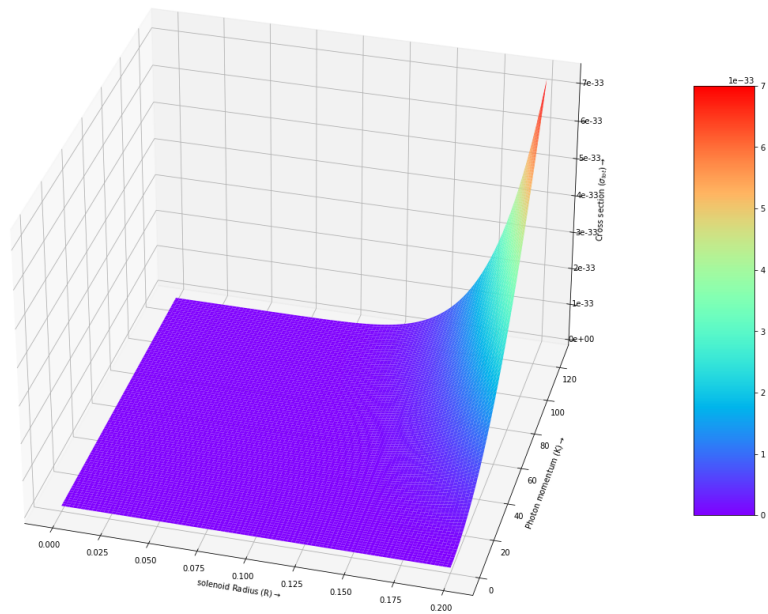


Figure 7.2(b) : surface.

A.1. 3D plots

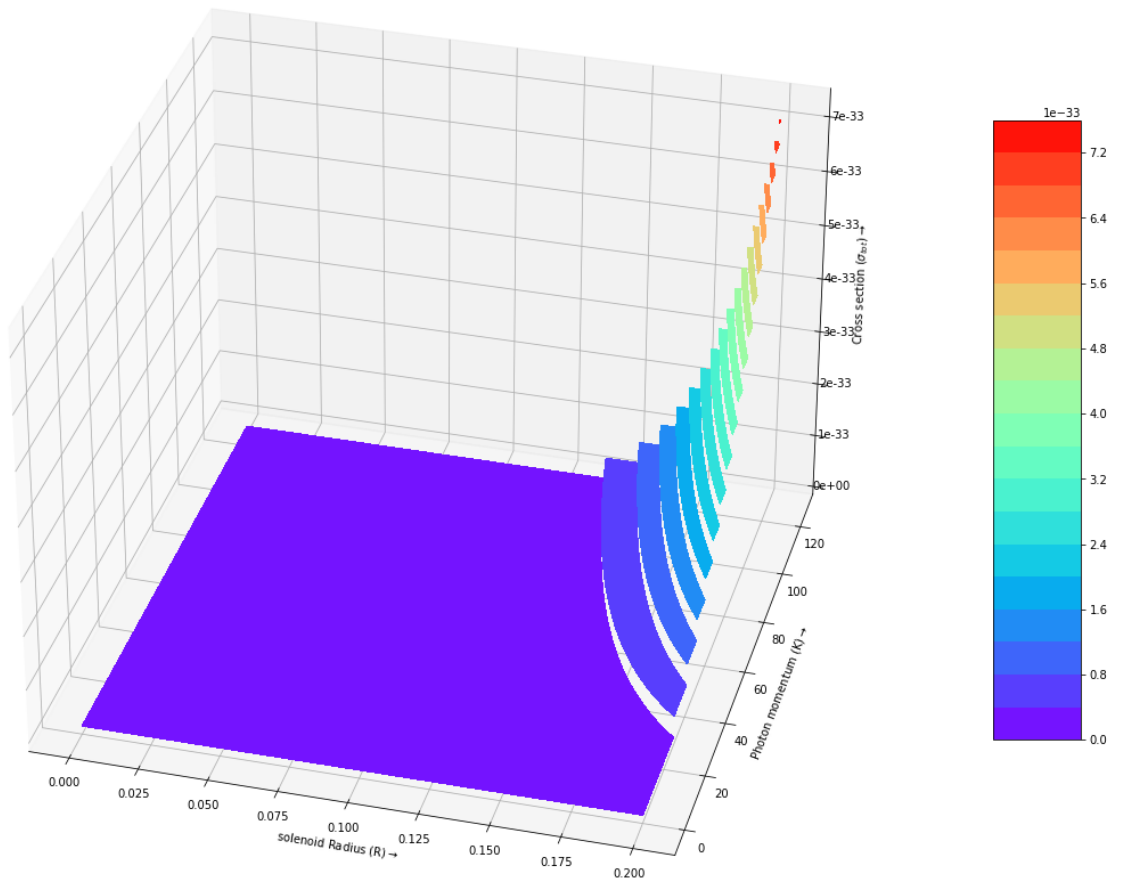


Figure 7.3(b) : contour.

A.1. 3D plots

A.1.3 σ_{tot} vs K vs B plot

PYTHON CODE :

```
#importing the essential libraries
from mpl_toolkits import mplot3d
import scipy.special as spl
import numpy as np
import matplotlib.pyplot as plt
import matplotlib.ticker as mtick

#assigning the constant values for the cross section plot;
w=124
L=10
g=8.8E-20
x=0.2

#defining our cross section function as z(x,y);
def z_function(B, y):
    return (np.sqrt(2*np.pi)*((y*L*g*B*(pow(x,2)))**2 * (1/16))*y*pow(
        x, 5)*np.exp(-(y**2)*(x**2))*
        spl.iv(0.5,(y**2)*(x**2)))

#defining our variables- B=x and K=y;
B = np.linspace(0, 1950, 100)
y = np.linspace(0, 125, 100)

#mapping the function z(x,y) to meshgrid Z(X,Y)
X, Y = np.meshgrid(B, y)
Z = z_function(X, Y)

#plotting wireframe plot Z(X,Y)
fig = plt.figure(figsize=(20,20))
ax = plt.axes(projection="3d")
ax.plot_wireframe(X, Y, Z, cmap='winter')
ax.view_init(32.5,-75)

#labeling the axis for wireframe
ax.set_xlabel('Magnetic field (B)' + r'$\rightarrow$')
ax.set_ylabel('Photon momentum (K)' + r'$\rightarrow$')
ax.set_zlabel('Cross section ( $\sigma_{tot}$ )' + r'$\rightarrow$')
plt.gca().zaxis.set_major_formatter(mtick.FormatStrFormatter('%0.0e'))
```

A.1. 3D plots

```
#fixing the figure size and zaxis format
fig = plt.figure(figsize=(20,20))
ax = plt.axes(projection='3d')
plt.gca().zaxis.set_major_formatter(mtick.FormatStrFormatter('%0e'))

#plotting Z(X,Y) with color bar
surf=ax.plot_surface(X, Y, Z, rstride=1, cstride=1,
                    cmap='rainbow', edgecolor='none')
fig.colorbar(surf,shrink=0.5,aspect=7)
ax.view_init(32.5,-75)
#labeling the axis for surface plot
ax.set_xlabel('Magnetic field (B)' + r'$\rightarrow$')
ax.set_ylabel('Photon momentum (K)' + r'$\rightarrow$')
ax.set_zlabel('Cross section ( $\sigma_{\text{tot}}$ )' + r'$\rightarrow$')

#fixing the figure size and zaxis format
fig = plt.figure(figsize=(20,20))
ax = plt.axes(projection="3d")
plt.gca().zaxis.set_major_formatter(mtick.FormatStrFormatter('%0e'))

#plotting Z(X,Y) with color bar
qcs=plt.contourf(X, Y, Z,20, cmap='rainbow')
plt.colorbar(qcs,shrink=0.5,aspect=7)
ax.view_init(32.5,-75)
#labeling the axis for countour plot
ax.set_xlabel('Magnetic field (B)' + r'$\rightarrow$')
ax.set_ylabel('Photon momentum (K)' + r'$\rightarrow$')
ax.set_zlabel('Cross section ( $\sigma_{\text{tot}}$ )' + r'$\rightarrow$')

#display our 3d plots
plt.show()
```

A.1. 3D plots

OUTPUT :

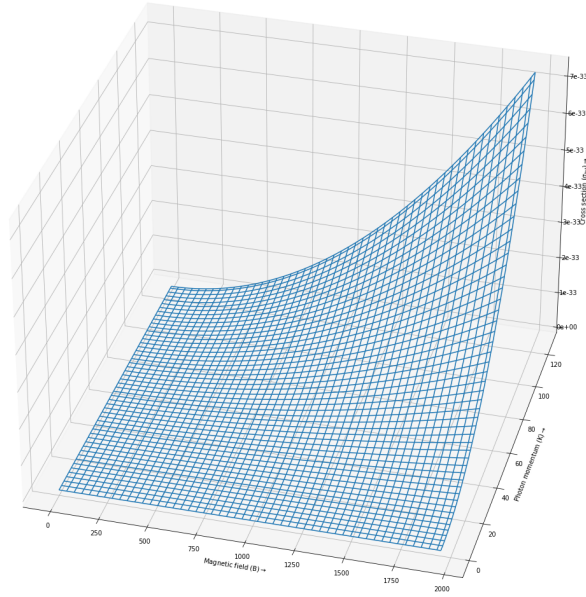


Figure 7.3(a) : wireframe.

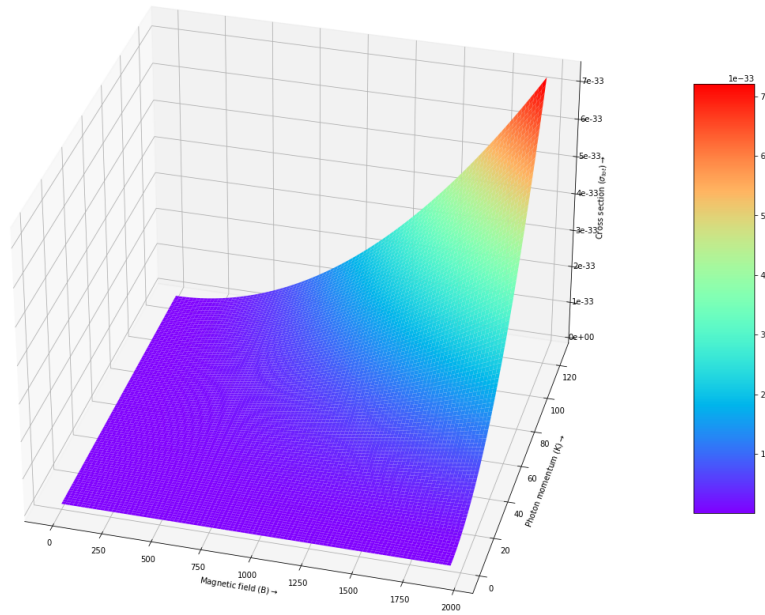


Figure 7.3(b) : surface.

A.1. 3D plots

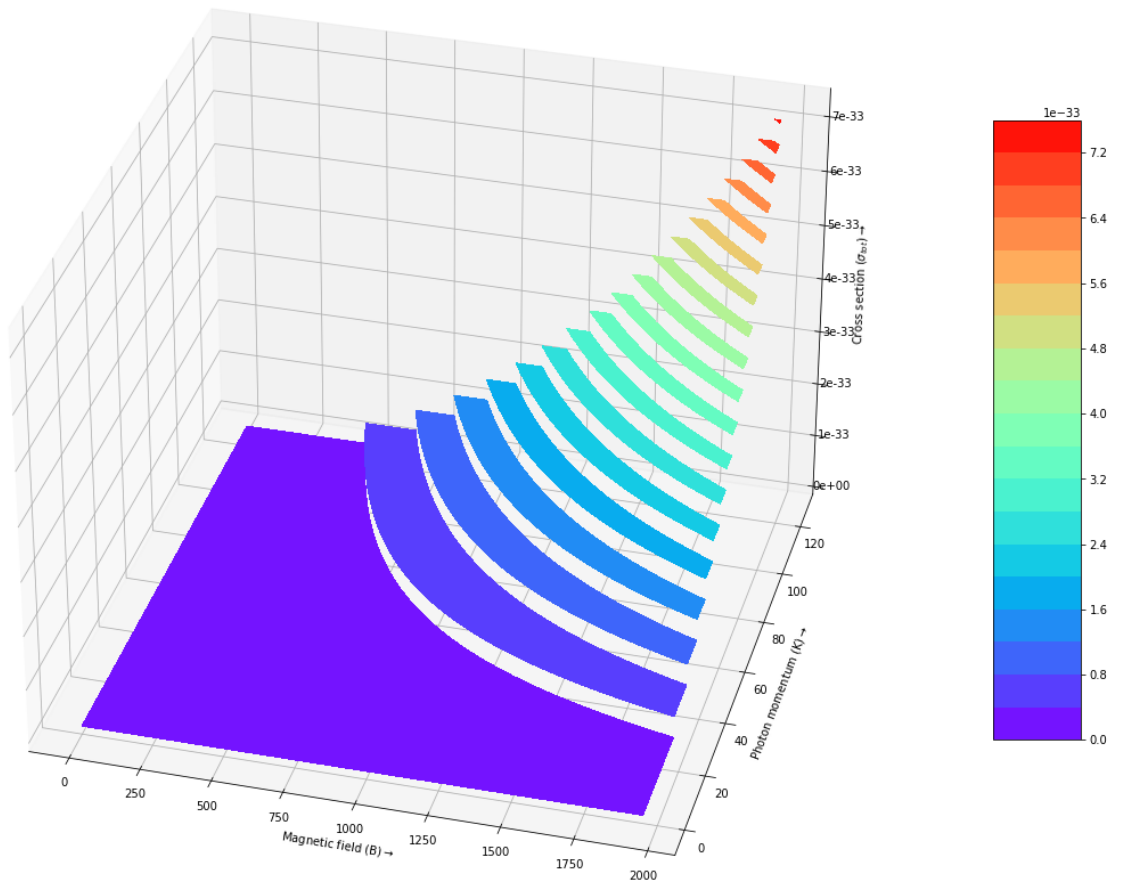


Figure 7.3(c) : contour.

A.2. 2D plots

A.2 2D plots

A.2.1 σ_{tot} vs K plot

PYTHON CODE :

```
#importing the essential libraries
from mpl_toolkits import mplot3d
import scipy.special as spl
import numpy as np
import matplotlib.pyplot as plt
import matplotlib.ticker as mtick

#assigning the constant values for the cross section plot;
B = 1950
w=124
L=10
g=8.8E-20
x = 0.2

#defining our cross section function as z(x,y);
def z_function(y):
    return (np.sqrt(2*np.pi)*((y*L*g*B*(pow(x,2)))**2 * (1/16))*y*pow(
        x, 5)*np.exp(-(y**2)*(x**2))*
        spl.iv(0.5,(y**2)*(x**2)))

#defining our variables- R=x and K=y;
y = np.linspace(0, 125, 50)
z=z_function(y)

#plotting wireframe plot Z(X,Y)
fig = plt.figure(figsize=(16,10))
plt.plot(y,z,'r-o')
plt.grid()

#setting the axis format and range
plt.gca().yaxis.set_major_formatter(mtick.FormatStrFormatter('% .1e'))
plt.yticks(np.arange(0, max(z), 0.5E-33))

# Setting axis labels for the plot
```


A.2. 2D plots

```
plt.ylabel('Cross section ( $\sigma_{tot}$ )'+ r'$\rightarrow$')
plt.xlabel('Photon momentum (K)'+ r'$\rightarrow$')

#display our 2D plots
plt.show()
```

OUTPUT :

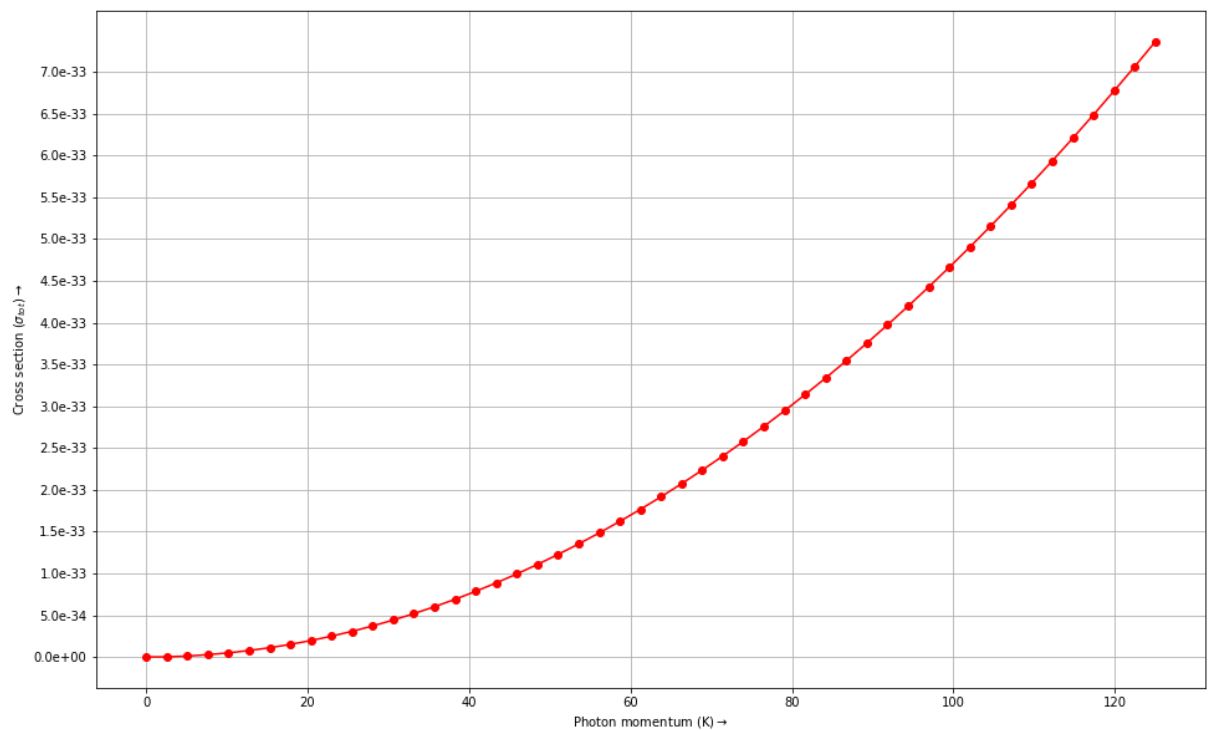


Figure 7.4 : σ_{tot} vs K plot .

A.2. 2D plots

A.2.2 σ_{tot} vs R plot

PYTHON CODE :

```
#importing the essential libraries
from mpl_toolkits import mplot3d
import scipy.special as spl
import numpy as np
import matplotlib.pyplot as plt
import matplotlib.ticker as mtick

#assigning the constant values for the cross section plot;
B = 1950
w=124
L=10
g=8.8E-20
y=124

#defining our cross section function as z(x,y);
def z_function(x):
    return (np.sqrt(2*np.pi))*((y*L*g*B*(pow(x,2)))**2 * (1/16))*y*pow(
        x, 5)*np.exp(-(y**2)*(x**2))*
        spl.iv(0.5,(y**2)*(x**2)))

#defining our variables- R=x and K=y;
x = np.linspace(0, 0.2, 50)
z=z_function(x)

#plotting wireframe plot Z(X,Y)
fig = plt.figure(figsize=(16,10))
plt.plot(x,z,'r-o')
plt.grid()

#setting the axis format and range
plt.gca().yaxis.set_major_formatter(mtick.FormatStrFormatter('%.1e'))
plt.yticks(np.arange(0, max(z), 0.5E-33))

# Setting x axis label for the plot
plt.ylabel('Cross section ( $\sigma_{tot}$ )' + r'$\rightarrow$')
plt.xlabel('Solenoid Radius(R)' + r'$\rightarrow$')

#display our 2D plots
```

A.2. 2D plots

```
plt.show()
```

OUTPUT :

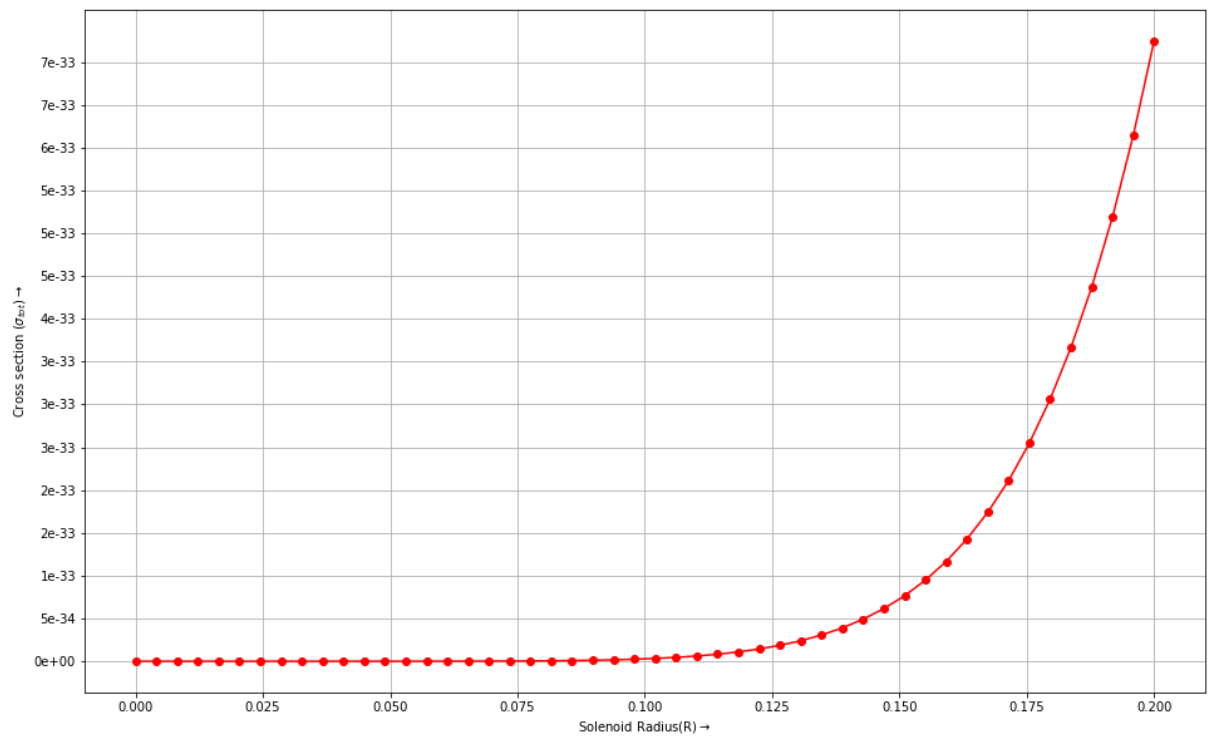


Figure 7.5 : σ_{tot} vs R plot .

APPENDIX B

Acronyms and Abbreviations

SM - Standard Model

QCD - Quantum Chromodynamics

P - Parity conjugation

C - Charge Conjugation

T - Time Reversal

PQ - Peccei and Quinn

WW - Weinberg and Wilczek

BBN - Big bang nucleosynthesis

WIMPs - Weakly Interacting Massive Particles

CDM - Cold Dark Matter

SSB - Spontaneous Symmetry Breaking

KSVZ - Kim-Shifman-Vainshtein-Zakharov

DFSZ - Dine-Fischler-Srednicki-Zhitnitskii

eV - Electron Volt

SNe Ia - Type Ia Supernova

CMB - Cosmic microwave background

CAST - CERN Axion Solar Telescope

SUMICO - Tokyo Axion Helioscope Experiment

ALP - Axion- Like Particles

PS-ALP - Psuedo Scalar ALP

S-ALP - Scalar ALP

RBF - Rochester-Brookhaven-Fermilab microwave cavity experiment

UF - University of Florida

ADMX - The Axion Dark Matter eXperiment

HFET - Heterojunction Field Effect Transistor

SQUID - Superconducting Quantum Interference Device

DM - Dark Matter

SN1987a - Type 2 Supernova

LHC - Large Hadron Collider

TPC - Time Projection Chamber

RHESSI - Reuven Ramaty High Energy Solar Spectroscopic Imager

HEMTs - High-Electron-Mobility Transistors

BNL - Brookhaven National Laboratory

RF - Radio Frequency

IF - Intermediate Frequency

FFT - Fast-Fourier transform

LHe - Liquid Helium

JPA - Josephson Parametric Amplifiers

CAPSEr - Cosmic Axion Spin Precession Experiment

NMR - Nuclear Magnetic Resonance

